Mineralium Deposita (2026) 61:699–726
https://doi.org/10.1007/s00126-025-01407-2

ARTICLE

Hyperspectral remote sensing study of the structurally-controlled Zn mineralization in the Flinders Ranges, South Australia

Anna Sorrentino[1] · **Saeid Asadzadeh**[2] · **Giovanni Camanni**[3] · **Francesco Carotenuto**[1] · **Sabine Chabrillat**[2,4] · **Sarah A. Gleeson**[2,5] · **Giuseppina Balassone**[1] · **Nicola Mondillo**[1,6]

Received: 20 January 2025 / Accepted: 3 November 2025 / Published online: 28 November 2025

Abstract

In this study, we investigate Zn mineralization in the Flinders Ranges, South Australia, using hyperspectral data from the Environmental Mapping and Analysis Program (EnMAP) satellite instrument to explore the spatial relationships between ore zones, hydrothermal alteration zones, and fault systems. Zinc mineralization in this area is hosted in Lower Cambrian lithologies and contains significant willemite, fraipontite, and Zn-phosphates, associated with extensive hematite- and dolomite-bearing hydrothermal alteration. Alteration mineral maps, showing relative abundance and compositional variations, were generated by applying a multiple-feature extraction methodology based on polynomial fitting and band ratios. Ground-truthing was conducted through laboratory spectroscopy and mineralogical-petrographic methods. This approach enabled the mapping of Fe oxy-hydroxides (i.e., hematite and goethite), carbonate minerals (i.e., dolomite and calcite), and dioctahedral phyllosilicates (i.e., white micas and kaolinite). It also successfully identified and mapped the ore mineral fraipontite based on its absorption feature at ~2260 nm. Multivariate statistical analysis and machine learning of the EnMAP imagery highlighted the co-occurrence of hematite, dolomite, and fraipontite in mineralized zones, making this assemblage a potential indicator for regional exploration of similar deposits. The study also revealed the controlling effects of fault structures on mineralization and the associated alteration haloes, with mineralized zones confined to fault-bounded rock volumes, predominantly located at intersections between interacting faults or in the proximity of lateral fault terminations. Overall, this work provides new insights into the spectral behavior of Zn-bearing minerals and demonstrates the effectiveness of hyperspectral sensing for characterizing oxidized Zn mineralization during regional prospecting programs.

Keywords VNIR-SWIR spectroscopy · EnMAP data · Mineral mapping · Dolomitization · Zn silicates · Structurally-controlled mineralization

Introduction

Several types of epigenetic ore deposits are associated with geological structures formed during crustal deformation, in particular, in association with faults, shear zones, and fracture systems (e.g., Cox et al. 2001; Sibson 2001; Walsh et al. 2018). This is because these structures and associated deformation can significantly enhance the host rock permeability, influencing both the fluid fluxes and fluid pressure (e.g., Cox et al. 2001; Cox 2005). Structurally-controlled oxidized Zn ores (also known as hypogene nonsulfide Zn deposits; Hitzman et al. 2003) mainly consist of Zn-silicates (dominantly willemite, with minor Zn-clays) in association with Zn-oxides (e.g., franklinite, zincite ± gahnite), precipitated by hydrothermal fluids, driven by fault systems, along structural traps (Hitzman

---

Editorial handling: M. Gadd

✉ Anna Sorrentino
anna.sorrentino2@unina.it

[1] Department of Earth, Environment and Resources Science, University of Naples “Federico II”, Naples, Italy

[2] GFZ Helmholtz Center for Geosciences, Telegrafenberg, Potsdam 14473, Germany

[3] Department of Chemical and Geological Sciences, University of Modena and Reggio Emilia, Modena, Italy

[4] Institute of Earth System Science, Department of Soil Science, Leibniz University Hannover, Hannover, Germany

[5] Research Ireland Centre in Applied Geosciences (iCRAG), School of Earth Sciences, University College Dublin, Dublin 4, Ireland

[6] Natural History Museum, London, UK

et al. 2003). Examples of such systems include Beltana and Aroona, in Australia (Groves et al. 2003), Vazante, in Brazil (Monteiro et al. 2006; Olivo et al. 2018), in addition to Kabwe and Star Zinc, in Zambia (Hitzman et al. 2003). Notably, the majority of these structurally-controlled ore deposits are associated with large-scale hydrothermal alteration haloes characterized by Fe-Zn-bearing dolomite and hematite, along with silicification, which can extend for several hundred meters from the mineralized body (Hitzman et al. 2003). Post-exhumation weathering can further complicate their mineralogy, forming several supergene minerals (e.g., smithsonite, hydrozincite, clays, Fe-hydroxides, etc.; Hitzman et al. 2003). Many of these hydrothermal and supergene minerals are spectrally active in the visible to near-infrared (VNIR) and short-wave infrared (SWIR) ranges (McConachy et al. 2007; Laukamp et al. 2021), making them highly suitable for detection by proximal and remote sensing systems (Sabins 1999; Taranik and Aslett 2009; Bedini 2017). Several investigations have been conducted at the regional scale on similar deposits, for example, in Iran and Morocco, by combining multispectral satellite data, including ASTER (Advanced Spaceborne Thermal Emission and Reflection Radiometer), Landsat 8, and Sentinel-2 A, as well as GeoEye-1 (Ghorbani et al. 2019; Chniouar et al. 2024; Honarmand et al. 2024; Hosseini et al. 2024). However, the larger spectral sampling distance of these sensors limits their ability to distinguish only a few broad compositional groups (Swayze et al. 2003). New-generation hyperspectral satellites, including DLR's (German Aerospace Center) EnMAP (Environmental Mapping and Analysis Program; Chabrillat et al. 2024) and DESIS (DLR Earth Sensing Imaging Spectrometer; Krutz et al. 2019), ASI's PRISMA (PRecursore IperSpettrale della Missione Applicativa; Cogliati et al. 2021), NASA's EMIT (Earth surface Mineral dust source Investigation; Green et al. 2020) among others, have increasingly made medium to high spectral resolution data, characterized by shorter spectral sampling distance, available to the scientific community (see Table A1 in the Electronic Supplementary Material, ESM, for a comparison of instrument specifics). The EnMAP system covers the spectral range between 420 and 2450 nm in 224 contiguous bands, at a spectral resolution of 6.5 nm and 10 nm with a signal-to-noise ratio of ≥400:1 and ≥250:1 in the VNIR and SWIR range, respectively, and at a 30 m spatial resolution (Guanter et al. 2015; Storch et al. 2023). This allows detailed discrimination of spectrally similar minerals compared to other hyper- and multispectral sensors (e.g., Asadzadeh et al. 2024; Chakraborty et al. 2024; Jain et al. 2024). However, the applicability and potential of EnMAP for mineral exploration purposes have yet to be fully demonstrated.

Fig. 1 Simplified regional geology map of the Flinders Ranges (modified from Dalgarno and Johnson 1966; Coats 1973; Preiss 1999). Locations of major Zn-Pb occurrences and structural corridors from Harkins et al. (2008) and Rowan and Vendeville (2006). The dashed black rectangles indicate the location of the maps shown in Fig. 2. The simplified cross-section along AA' shown at the bottom is modified from Rowan and Vendeville (2006) ▶

The present study focuses on investigating the spectral response of alteration and Zn-bearing mineral phases associated with structurally-controlled, oxidized, Zn mineralization located in the Flinders Ranges, South Australia (Fig. 1), through the use of the EnMAP satellite data and laboratory hyperspectral analyses on a set of samples from the study area. The work aims to assess the effectiveness of EnMAP and proximal data in the spectral detection and characterization of gangue and ore minerals occurring within these deposits and to examine the spatial relationships between hydrothermal alteration, ore zones, and fault structures. The Flinders Ranges include two main mineralized areas, the Beltana and the Reaphook districts (Groves et al. 2003; Harkins et al. 2008), which have not been previously investigated through spectral sensing. The results are compared with previous studies conducted on similar deposits in other parts of the world.

Geology and tectonic evolution of the Flinders Ranges

The region of the Flinders Ranges covers an area of 500 km^2 in South Australia, in the northern part of the Adelaide Fold Belt, which formed in response to the deformation of the Adelaide Basin (Preiss 2000; Harkins et al. 2008). This Late Proterozoic to Middle Cambrian sedimentary basin evolved from an initial stage of continental rifting into a passive margin setting, resulting in the deposition of a 15 km-thick succession of siliciclastic and shallow to deep-water carbonate sedimentary rocks (Thomson 1976). The oldest rocks deposited within the sedimentary basin belong to the Neoproterozoic Callanna Group, and comprise basal volcano-clastic units followed by carbonates and evaporites (Fig. 1). The Callanna Group is overlain by quartzites, shales, and carbonate rocks of the Neoproterozoic Burra, Umbertana, and Wilpena Groups (Preiss 2000; Harkins et al. 2008; Cowley 2020). The basal part of the Cambrian succession begins with the Parachilna Formation, a sequence of sandstones, quartz arenites, and siltstones that passes upward into the Ajax Limestone with a gradational contact. The Ajax Formation is a carbonate platform succession, subdivided into three members: the Woodelinna Dolomite, the Lower Wilkawillina Limestone, and the Upper Wilkawillina Limestone (Groves et al. 2003; Harkins et al. 2008; Cowley 2020). The overlying Cambrian

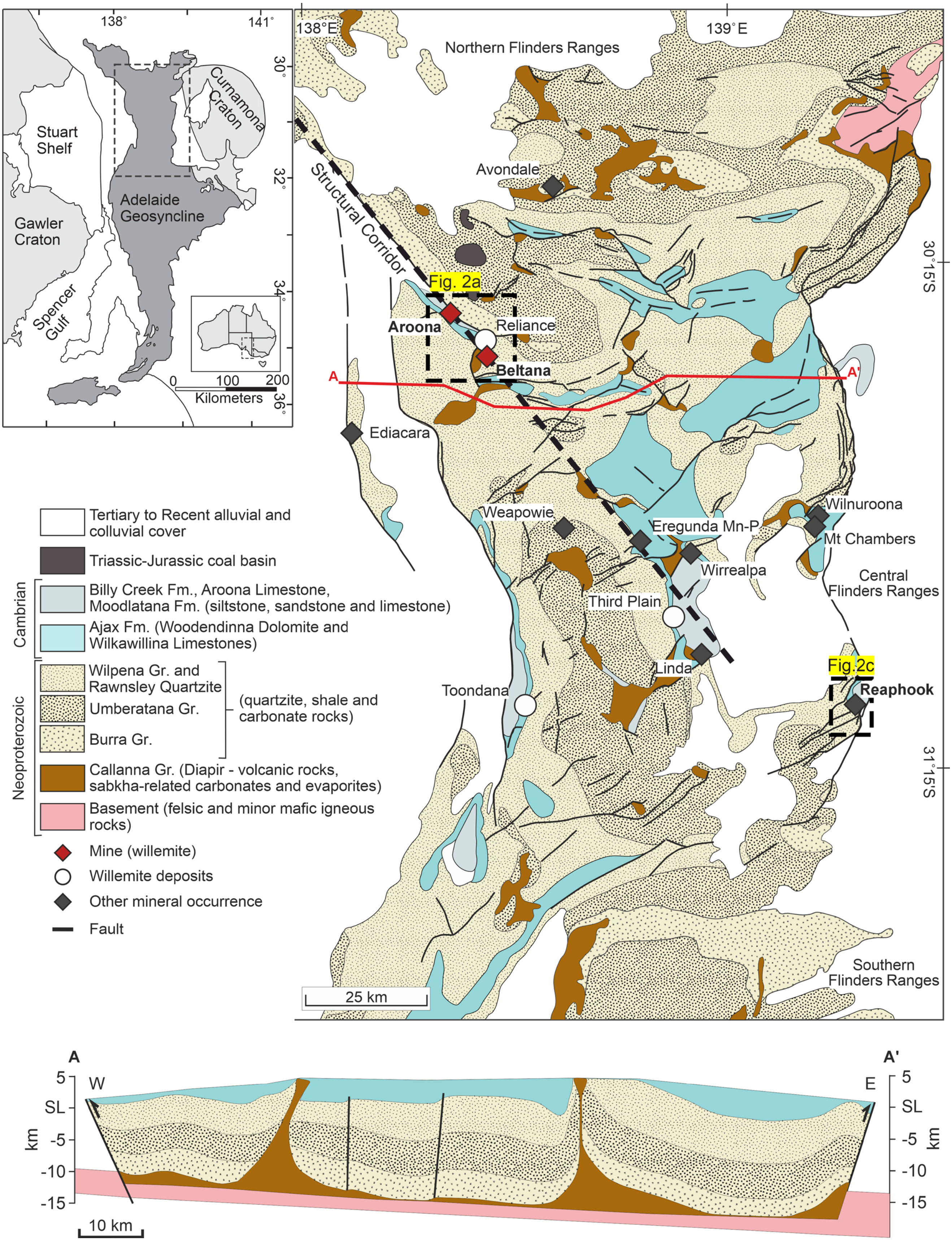
138°
141°
30°
32°
34°
36°
Stuart Shelf
Curnamona Craton
Adelaide Geosyncline
Gawler Craton
Spencer Gulf
0 100 200
Kilometers
138°E
139°E
Northern Flinders Ranges
Avondale
Structural Corridor
Fig. 2a
Aroona
Reliance
Beltana
A
A'
Ediacara
30°15'S
Weapowie
Eregunda Mn-P
Wilnuroona
Mt Chambers
Wirrealpa
Central Flinders Ranges
Third Plain
Linda
Toondana
Fig.2c
Reaphook
31°15'S
Southern Flinders Ranges
25 km
Tertiary to Recent alluvial and colluvial cover
Triassic-Jurassic coal basin
Cambrian
Billy Creek Fm., Aroona Limestone, Moodlatana Fm. (siltstone, sandstone and limestone)
Ajax Fm. (Woodendinna Dolomite and Wilkawillina Limestones)
Neoproterozoic
Wilpena Gr. and Rawnsley Quartzite
Umberatana Gr.
Burra Gr.
(quartzite, shale and carbonate rocks)
Callanna Gr. (Diapir - volcanic rocks, sabkha-related carbonates and evaporites)
Basement (felsic and minor mafic igneous rocks)
Mine (willemite)
Willemite deposits
Other mineral occurrence
Fault
A
A'
W
E
5
SL
-5
-10
-15
km
10 km

sedimentary rocks are represented by the red beds of the Billy Creek Formation, by the shaly Moodlatana Formation, and finally by the Aroona Creek Limestone (Groves et al. 2003; Harkins et al. 2008).

The sedimentary basin underwent a phase of tectonic inversion, associated with both thin- and thick-skinned deformation during the Delamerian orogenesis, which is interpreted to have begun in the Late Cambrian–Ordovician (Preiss 2000; Dyson 2001; Foden et al. 2006; Cowley 2020), or since the Late Neoproterozoic to Early Cambrian (Jenkins 1990; Rowan and Vendeville 2006). The contractional deformation in the Flinders Ranges resulted in structural trends with varying orientations in different zones of the belt: from NW-SE, E-W, to NE-SW-trending folds in the North Zone, through dome-and-basin structures in the Central Zone, to N-S to E-W-trending folds in the South Zone (Rutland et al. 1981; Preiss 2000; Rowan and Vendeville 2006). One of the most relevant features of the Flinders Ranges is the occurrence of broad antiformal domes of the Callanna Group evaporites that intrude the overlying Neoproterozoic and Lower Cambrian sedimentary sequences and have been interpreted as diapirs. In outcrop, these bodies consist of carbonate breccias representing the top of deeper salt bodies. The diapirism of the Callanna Group evaporites took place in a syn-depositional fashion, due to sediment loading, well before the Delamerian orogeny. The Delamerian deformation style has been strongly influenced by the occurrence of diapirs. Specifically, almost all anticlines and faults intersect diapirs, and most diapirs have two or more anticlines plunging away from them in different directions (Fig. 1; Rowan and Vendeville 2006).

Most of the Zn ores in the Flinders Ranges are hosted by limestone of the Lower Cambrian Ajax Formation or more rarely in the underlying Early Cambrian Parachilna Formation and Neoproterozoic Burra limestone, and consist of willemite, Zn-clays, coronadite, and Zn-Pb arsenates in a gangue of hydrothermal hematite and dolomite (Fig. 1; Groves et al. 2003; Harkins et al. 2008). The mineralization predominantly occurs in structurally-controlled bodies that are in contact with the Callanna Group diapirs (Harkins et al. 2008). For this reason, it was proposed that the Callanna Group diapirs and their nearby structures played a key role in controlling the mineralization, likely serving as vertical conduits for metal-bearing hydrothermal brines (Brugger et al. 2003; Harkins et al. 2008). K-Ar dating of coronadite from Beltana yielded Ordovician ages 437 ± 5 Ma and 430 ± 5 Ma, suggesting that Zn mineralization in the Flinders Ranges was related to exhumation that post-dated Delamerian orogenesis (Groves et al. 2003).

Fig. 2 **a** Simplified geology map of the Beltana – Aroona district (modified from Coats 1973). **b** Enlargement of the dashed yellow rectangle showing a detailed geology map of the Beltana mining area (modified from Groves et al. 2003). **c** Simplified geology map of the Reaphook Hill (modified from Dalgarno and Johnson 1966; Preiss 1999). Location and names of the mineral deposits (yellow diamonds) from the Geoscience Australia Portal (https://portal.ga.gov.au/). The positions of the collected hand samples are shown by black dots

The Beltana – Aroona district and the Reaphook prospect

The Beltana – Aroona district, in the northern Flinders Ranges, contains high-grade hypogene willemite deposits (estimated resource in 2003 of 8.6 Mt at 37.9% Zn at Beltana and 1.5 Mt at 34.4% Zn at Aroona), located within a 15-km-long northwest-trending structural corridor, delimited by the northwest trending faults (Fig. 2a; Carman and Groves 2003). The mineralization is hosted in carbonate rocks of the Cambrian Ajax Formation, and is associated with pervasive hydrothermal dolomitization and hematitization. The spatial distribution of deposits is controlled by major brittle structures and hydrothermal collapse breccias (Groves et al. 2003; Harkins et al. 2008). The hydrothermal alteration preceded the mineralization event (Groves et al. 2003). The Beltana orebody crops out at the surface as several occurrences over a distance less than 0.5 km (Fig. 2b), located in the footwall of the north-trending Beltana thrust Fault, which marks the boundary between the diapiric Callanna Group and the Ajax Limestone host rock (Fig. 2a and b; Muller 1972; Harkins et al. 2008). The Aroona deposits are smaller in tonnage and shallower in depth and occur in a narrow fault wedge between the major Northwest Fault and the minor Aroona Fault in the Woodendinna Dolomite (Fig. 2a; Carman and Groves 2003). Willemite is the main zinc ore mineral occurring in various types of textures, such as (i) massive fine-grained red willemite, resulting from the direct replacement of the host rock; (ii) finely laminated and/or zebra red and white willemite, deposited as internal sediments in solution cavities; and (iii) well-crystallized multi-phase crustiform and colloform willemite, in open-space fillings. Zinc clays are intimately associated with the mineralization. Minor Pb-bearing minerals, including coronadite, hedyphane, and mimetite formed during the late stages of the paragenesis and occur in vein and fracture networks cross-cutting willemite and as vug infills (Muller 1972; Carman and Groves 2003; Groves et al. 2003; Harkins et al. 2008). Sulfides are completely absent in the orebodies (Groves et al. 2003).

The Reaphook prospect is located approximately 100 km southeast of Beltana (Fig. 1), and hosts several rare zinc phosphate minerals, clustered in three separate near-surface mineralized zones as shown in Fig. 2c. The mineralization

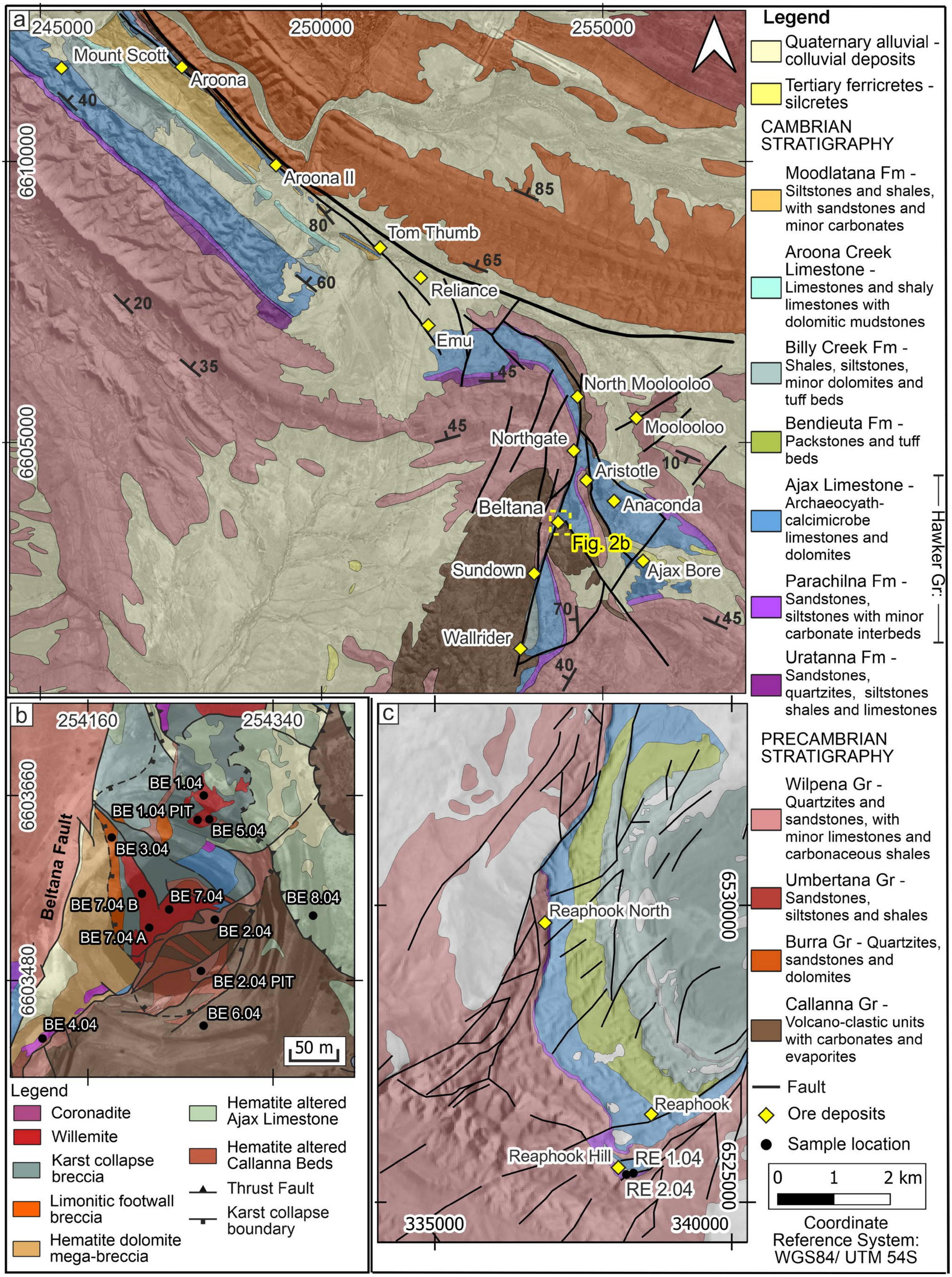
a
245000
250000
255000
6610000
6605000
Mount Scott
Aroona
Aroona II
Tom Thumb
Reliance
Emu
North Moolooloo
Moolooloo
Northgate
Aristotle
Beltana
Anaconda
Fig. 2b
Sundown
Ajax Bore
Wallrider
40
80
85
65
60
20
35
45
45
10
70
45
40
Legend
Quaternary alluvial - colluvial deposits
Tertiary ferricretes - silcretes
CAMBRIAN STRATIGRAPHY
Moodlatana Fm - Siltstones and shales, with sandstones and minor carbonates
Aroona Creek Limestone - Limestones and shaly limestones with dolomitic mudstones
Billy Creek Fm - Shales, siltstones, minor dolomites and tuff beds
Bendieuta Fm - Packstones and tuff beds
Ajax Limestone - Archaeocyath-calcimicrobe limestones and dolomites
Parachilna Fm - Sandstones, siltstones with minor carbonate interbeds
Hawker Gr.
Uratanna Fm - Sandstones, quartzites, siltstones shales and limestones
PRECAMBRIAN STRATIGRAPHY
Wilpena Gr - Quartzites and sandstones, with minor limestones and carbonaceous shales
Umbertana Gr - Sandstones, siltstones and shales
Burra Gr - Quartzites, sandstones and dolomites
Callanna Gr - Volcano-clastic units with carbonates and evaporites
Fault
Ore deposits
Sample location
0 1 2 km
Coordinate Reference System: WGS84/ UTM 54S
b
254160
254340
6603660
6603480
Beltana Fault
BE 1.04
BE 1.04 PIT
BE 5.04
BE 3.04
BE 7.04 B
BE 7.04
BE 8.04
BE 7.04 A
BE 2.04
BE 2.04 PIT
BE 6.04
BE 4.04
50 m
Legend
Coronadite
Willemite
Karst collapse breccia
Limonitic footwall breccia
Hematite dolomite mega-breccia
Hematite altered Ajax Limestone
Hematite altered Callanna Beds
Thrust Fault
Karst collapse boundary
c
Reaphook North
Reaphook
Reaphook Hill
RE 1.04
RE 2.04
6530000
6525000
335000
340000

is hosted within the Lower Cambrian Parachilna Formation and is considered a supergene remnant of weathered primary minerals (Harkins et al. 2008; Elliott 2022). The ore minerals are mainly scholzite with minor tarbuttite, associated with extensive surficial ferruginous and manganiferous caps (Groves et al. 2003). The phosphate minerals in mineralized zones occur as vug-fillings in the form of both euhedral and intricately intergrown anhedral crystals, with the main mineral phase, scholzite, forming radiating prismatic needles or white fibers (Hill 1973; Hill and Milnes 1974). The mineralization is associated with intense hematite and dolomite alteration (Harkins et al. 2008).

Materials and methods

Hand sample mineralogical and spectroscopic analyses

Fourteen hand samples collected from the Beltana open-pit and the Reaphook prospect (available at the Ore Deposits mineral collection at the University of Naples) were used for laboratory mineralogical and spectroscopic analyses. The samples comprise different lithologies, including carbonate host rocks, hydrothermal facies, and mineralized zones (sample locations are shown in Fig. 2b and c).

X-ray diffraction (XRPD) and field emission scanning electron microscope (FESEM-EDS) analyses were conducted at the University of Naples, DiSTAR (Italy). Parts of the samples were ground to produce ~ 10 g of powder for bulk X-ray diffraction analysis (XRPD). Specific XRPD analyses were also conducted on hand-picked samples of the clay-rich matrix of the mineralized breccias. The XRPD analysis was carried out by using a Seifert-GE diffractometer ID 3003. Intensity profiles were collected in the range from 3° to 80° 2θ using Ni-filtered CuKα radiation at 40 kV and 30 mA, with a step size of 0.02° and a scanning time of 10 s/step. Microchemical analyses on polished thin sections were carried out using FESEM-EDS Zeiss Merlin VP Compact and JEOL JSM-5310 coupled with Oxford Instruments Microanalysis Unit equipped with an INCA X-act solid-state detector. Data sets were obtained using an INCA X-max processor (15 kV primary beam voltage, 50–100 A filament current, 20 mm working distance, and 50 s real-time counting) by means of INCA Energy software 5.05 (XPP array and pulse pile-up corrections). Optimization of signals was carried out using cobalt (FWHM peak height of the strobed zero = 60–65 eV) as a reference. The standard materials from the Smithsonian Institute and MAC (Micro-Analysis Consultants Ltd., Saint Ives, UK) were used for calibration. Because of the Na-Zn peaks' overlap in the energy-dispersion spectrum, the Na content was not measured in the Zn-clays (see Mondillo et al. 2015).

The spectroscopic measurements were carried out on flat slab samples from the counterpart of thin-sections, and on the Zn-clay concentrates, at the Spectroscopy Laboratory of the German Research Centre for Geosciences (GFZ) in Potsdam, using the Analytic Spectral Devices (ASD) FieldSpec-4 Standard-Res spectroradiometer (https://www.malvernpanalytical.com). The ASD FieldSpec-4, equipped with a contact probe with a built-in light source, collects data in 2151 spectral bands from 350 to 2500 nm, with a spectral resolution of 3 nm in the VNIR and 10 nm in the SWIR. A Spectralon® panel was used as a white reference to convert the raw data into reflectance. The instrument was set up to average 50 consecutive measurements for each record, and at least four spectra were collected per sample. The visualization, analysis, and interpretation of the resulting spectral data were performed using the ENVI (v5.6.2) software and the USGS spectral library (Kokaly et al. 2017) as a reference. We also used the spectral library described in McConachy et al. (2007) to identify Zn-bearing minerals. On this basis, a custom spectral library was developed to interpret the collected spectral data.

The same sample collection was subsequently scanned using HySpex's hyperspectral imaging cameras VNIR-1600 and SWIR-320 m, to obtain textural information of spectrally active minerals. The HySpex's scanning system covers the spectral range between 400 and 2500 nm, with a spectral resolution of 3.7 nm in the VNIR and 6 nm in the SWIR (https://www.hyspex.com/). The samples were illuminated by two halogen lamps at an angle of ~45°. After dark current subtraction, the collected data were calibrated to radiance using camera-specific radiometric factors and then converted to reflectance using three reference panels (20%, 50%, and 90% reflectivity), selected according to the albedo of the samples. The high-resolution imaging data were pre-processed using the ENVI software, which involved manual masking to remove the background tray, stacking the VNIR and SWIR data using manually selected tie points, and spectral smoothing through the Savitzky-Golay filter (Savitzky and Golay 1964) with the width and polynomial degree set to 2.

EnMAP satellite data collection and processing

The EnMAP hyperspectral satellite data were acquired on December 31 st, 2023, at 10:33:28 (local time) for the Beltana - Aroona area (Sun Elevation Angle 71.59 and Sun Azimuth Angle 70.30), and on January 11th, 2024, at 10:19:25 (local time) for the Reaphook prospect (Sun Elevation Angle 67.59 and Sun Azimuth Angle 70.37). These datasets were downloaded from the EOWEB® GeoPortal in BSQ format and consisted of "surface reflectance Level 2A products", which are orthorectified, atmospherically corrected reflectance data. The 30 × 30 km scenes were clipped to the areas of interest and the noisy bands occurring between 1342 and

1390 nm and from 1780 to 1967 nm, due to strong atmospheric water vapor absorptions and set to background values in the L2A data, were removed from each data cube (e.g., Tan et al. 2020). Finally, to reduce the noise in the VNIR sub-system, which is dominated by broad Fe-related absorptions, the wavelength range between 770 and 1080 nm was spectrally smoothed using a boxcar filter with a width size of 7 nm (e.g., Asadzadeh et al. 2024; Laukamp et al. 2021).

Spectral signatures and mineral mapping

Spectral processing included a combination of band ratio calculations and polynomial fitting techniques implemented in the Interactive Data Language (IDL) environment, to enable the characterization of distinct absorption features. Polynomials of second to fourth order were fitted to specific wavelength intervals over which the local continuum was removed initially, to determine the wavelength position (also known as minimum wavelength) of the desirable absorption features in each image pixel (see Rodger et al. 2012; Asadzadeh and Souza Filho 2016). Beyond the minimum wavelength, the technique retrieves the depth, width, and asymmetry of the features, enabling the detection of mineralogy, chemical variations, relative abundance, and crystallinity of target minerals. By plotting the retrieved spectral parameters in scatterplots, the distribution of each mineral is mapped over the area. This methodology was applied to images acquired in the lab by the HySpex imaging system and the EnMAP satellite. The scripts employed to map the relative abundance (D index) and chemical composition (W index) for each target mineral are reported in Table 1. Further details on data processing, wavelength selection, and polynomial fitting order are described in the Electronic Supplementary Material (ESM).

Table 1 Spectrally detected minerals in the Beltana-Aroona and Reaphook study areas along with the spectral index used to identify them. "D" refers to the feature depth at wavelength λ, and "W" to the minimum wavelength of the same feature. The mineralogical information derived from scanned hand samples and EnMAP hyperspectral data are distinguished from each other. The table summarizes the diagnostic absorption features of the minerals and the scripts used for their detection and characterization, adopted and modified form the cited literature

Mineral Group	Mineral species	Diagnostic absorption features (nm)	Identifier Index	Detection script	References
Mineral phases detected on samples and on the regional scale					
Fe oxy-hydroxides	hematite, goethite	broad Fe^{3+} absorption (CFA) between 870 (hematite) - 940 (goethite)	900D	Band ratios $(R_{770}+R_{1080})/(R_{870}+R_{940})$ and $(R_{620}+R_{690})/(R_{480}+R_{550})$, applied after a spectral smoothing Boxcar filter (width = 7nm)	(Cudahy et al. 2008; Thiele et al. 2021)
			900W	Band ratio (R_{940}/R_{870})	
Carbonates	calcite, dolomite	$3v_3CO_3$ absorption between 2300 - 2340 nm	2330D 2330W	Fitted 4th-order polynomial between 2300 - 2370 nm (continuum removal between 2241 to 2392 nm)	(Chirico R et al., 2022; Laukamp et al. 2012)
Di-octahedral sheet silicates	white mica	Al-OH absorption between 2185 (Al-rich) - 2215 (Al-poor) nm and minor 2350 nm	2200D 2200W	Fitted 2nd-order polynomial between 2182 - 2224 nm (continuum removal between 2122 - 2249 nm), absence of ~ 2160 nm feature and presence of ~ 2350 nm	(Asadzadeh et al. 2024; Van Ruitenbeek et al. 2014)
	kaolinite group	Al-OH double absorption at 2165 and 2205 nm	2165D	Fitted 2nd-order polynomial between 2155 - 2170 nm (continuum removal between 2122 - 2249 nm), isolated with 2200D vs 2165D scatter plot	(Haest et al. 2012; Asadzadeh et al. 2024)
Tri-octahedral sheet silicates	*fraipontite	Zn-OH absorption between 2250 and 2265 nm	2260D	Fitted 2nd-order polynomial between 2250 - 2280 nm (continuum removal between 2200 - 2300 nm)	(e.g., Laukamp et al. 2012; Sonntag et al. 2012)
Mineral phases detected exclusively on the hand samples					
Zn phosphates	tarbuttite	Zn-OH absorptions at 2300 and 2370 nm	2370D	Fitted 2nd-order polynomial between 2360 - 2380 nm (continuum removal between 2300 - 2500 nm), constrained by the 2300 nm feature	(McConachy et al. 2007)
	scholzite	Zn-OH absorption at 2430 nm	2430D	Fitted 2nd-order polynomial between 2400 - 2450 nm (continuum removal between 2300 - 2500 nm), constrained by the 1480 nm feature	(McConachy et al. 2007)
Arsenates	-	OH and H_2O absorptions between 1400 - 1450 nm and 1900 - 1950 nm	1440D	Fitted 2nd-order polynomial between 1410 - 1450 (continuum removal between 1300 - 2000 nm)	(McConachy et al. 2007)
			1940D	Fitted 2nd-order polynomial between 1910 - 1950 (continuum removal between 1300 - 2000 nm)	(McConachy et al. 2007)

*mineral phases spectrally detected for the first time on the analyzed samples

The mineral maps of the samples were depicted with different color codes for each mineral type (or mineral mixtures). In contrast, the satellite individual mineral maps were displayed with a rainbow color gradient. To assess the significance of the relative abundance mineral maps (D), a minimum threshold was determined. By plotting in a histogram the depth values of each pixel extracted from the band ratios or polynomial fitting, it appears that the data have a bell-shaped distribution with a positively skewed tail. The point of maximum curvature on the right-hand side of the maximum was considered the optimal threshold for distinguishing the significant spectral features (Corrado et al. 2025; Sorrentino et al. 2024). Minimum and maximum values on the color scale of the absorption wavelength position (W) were represented by the corresponding extreme minimum and maximum values in the considered band. The results were overlain on an albedo image for visual enhancement. Similarly to previous studies (e.g., see Corrado et al. 2025; Sorrentino et al. 2024), to verify the quality of the satellite data in detecting the mineralization features (alteration haloes and ore minerals) and to asses that the mapped absorption features were truly present in the satellite spectra, selected spectra were extracted from image pixels and were compared to both the resampled spectra of pure mineral phases taken from the world-known USGS spectral library (Kokaly et al. 2017) and to the high-resolution spectra collected by the ASD spectroradiometer on ground samples. Although the ground samples mostly derive from individual mining sites and are not widespread in the region, the interpretation of the spectral mineral maps at the regional scale was possible due to the presence of very detailed geological maps reporting the distinct outcropping lithofacies (available at "https://portal.ga.gov.au/").

Multivariate analyses and machine learning-based EnMAP reconstruction

For this study, multivariate statistical analysis was carried out on the EnMAP spectral mineral maps to quantitatively determine the relationships between the distinct spectral signatures, with the addition of machine learning. Specifically, a first principal component analysis (PCA) was conducted on the absolute x, y, z_n values, with z_n corresponding to: white mica relative abundance map (2200D index), kaolinite relative abundance map (2165D index), carbonates relative abundance map (2330D index), Ferric iron relative abundance map (900D index) and the 2260 nm feature depth map (2260D index), likely corresponding to the fraipontite relative abundance. A second PCA was conducted on a modified database which included in the z_n the relative abundances of calcite and dolomite, calculated by using the relative shift of the feature at 2330 nm and the corresponding feature depth map (2330D index), the relative abundances of goethite and hematite, calculated by using the band ratio (R_{940}/R_{870}) and the 900D index map, and the feature abundance maps of white mica, kaolinite and fraipontite. The principal component analyses were performed using the *princomp* and *terra* packages from the Comprehensive R Archive Network (CRAN), through the R software. Results were shown by using biplots and maps of the significant PCn.

The EnMAP data were further processed by the Extreme Gradient Boosting (XGBoost) machine learning algorithm (Chen and Guestrin 2016; Hajaj et al. 2024; Lin et al. 2023), as a trial to automatically predict the most probable lithofacies and mineralized facies of the study area. More specifically, we used the Beltana mining area to create the training dataset, including the spectral features of the following lithofacies classes: limestones, dolomites, silico-clastic cover, carbonate cover, goethite-rich soil, hematite-rich soil, and mineralized zones. For this multiclass classification problem, the algorithm XGBoost iteratively combines multiple decision trees by discarding those not increasing the algorithm's predictive performance. The best model is the one including an ensemble of decision trees that minimizes both the prediction error and the model's complexity to have a good prediction performance while reducing overfitting.

Since our dataset was not balanced (i.e., the number of observations is very different from one class to another), we resampled the original training dataset 100 times by randomly sampling a number of observations per class equal to the number of observations in the poorest one (the "mineralized zone" class with 40 observations). This means that we created 100 training datasets used to feed 100 XGBoost models. The parameters characterizing each one of these models were optimized by using a 5-fold cross-validation procedure. We selected another dataset with well-known mineralization in the south of the Beltana area as the testing dataset and used the Confusion Matrix strategy to measure the predictive performance of these 100 models using accuracy metrics. In the end, we applied the 100 XGBoost models on the spectral products to give rise to 100 maps of the areas with cells, each one indicating the probability of having one of the lithofacies. We then averaged these maps after weighting them by using the accuracy values of their corresponding models. The final map was the one in which the most probable class to every cell is assigned. Once creating the maps of the class distributions, we overlapped them with the geological map (shown in Fig. 2a) and computed the percentage of predicted lithofacies classes in each geological formation. We implemented the XGBoost algorithm and the models' performance measures by using the *caret* package (Kuhn 2008), whereas raster data was handled by using the *terra* package (Hijmans 2025) available in R (R Core Team 2024).

Results

XRD and SEM-EDS mineralogical analyses on ground samples

The breccia sample BE 3.04 comprises dolomite clasts that are cemented by hematite and minor goethite. Hematite also occurs as inclusions within dolomite. Dolomite is locally zincian (e.g., Fig. 3a and b). The quartzite sample BE 2.04 is characterized by quartz and K-feldspar replaced by muscovite along rims, with hematite and dolomite crystals precipitated along fractures and in the rock pores (see Fig. 3c).

The mineralized sample BE 7.04 is a breccia composed of broken and rotated clasts of host rock replaced by granular and fine-grained red willemite and cemented by well-crystallized white willemite and coronadite. Willemite takes on reddish tones when hematite micro-inclusions are present, whereas white willemite has no impurities. Other minor mineral phases detected include Zn-clays, together with calcite, and trace Zn- and Pb-arsenates (see Fig. 3d and e). Sample BE 7.04 A shows laminated red willemite and crustiform white willemite that occurs as aggregates of hexagonal prism crystals in cavities associated with Zn-clays and minor smithsonite (see Fig. 3f). Specific XRPD and FESEM-EDS analyses (Table 2) indicate that Zn-clays mostly consist of fraipontite, which was not reported in previous studies conducted on the deposit. Indeed, bulk XRPD patterns obtained on the clay-rich matrix are characterized by the typical reflections with a 7.03 Å basal spacing (001) and a further 3.52 Å (002) in association with a subtle broad peak at ca. 14.8–15 Å possibly indicating the co-occurrence of smectite or chlorite (Fig. 4a). In addition, the FESEM-EDS analyses of the Zn-clay-rich material resulted in average concentrations of 24.98 wt% SiO_2, 15.70 wt% Al_2O_3, and 40.92 wt% ZnO with lower MgO amounts of 5.64 wt% (Table 2). A limited number of analyses yielded

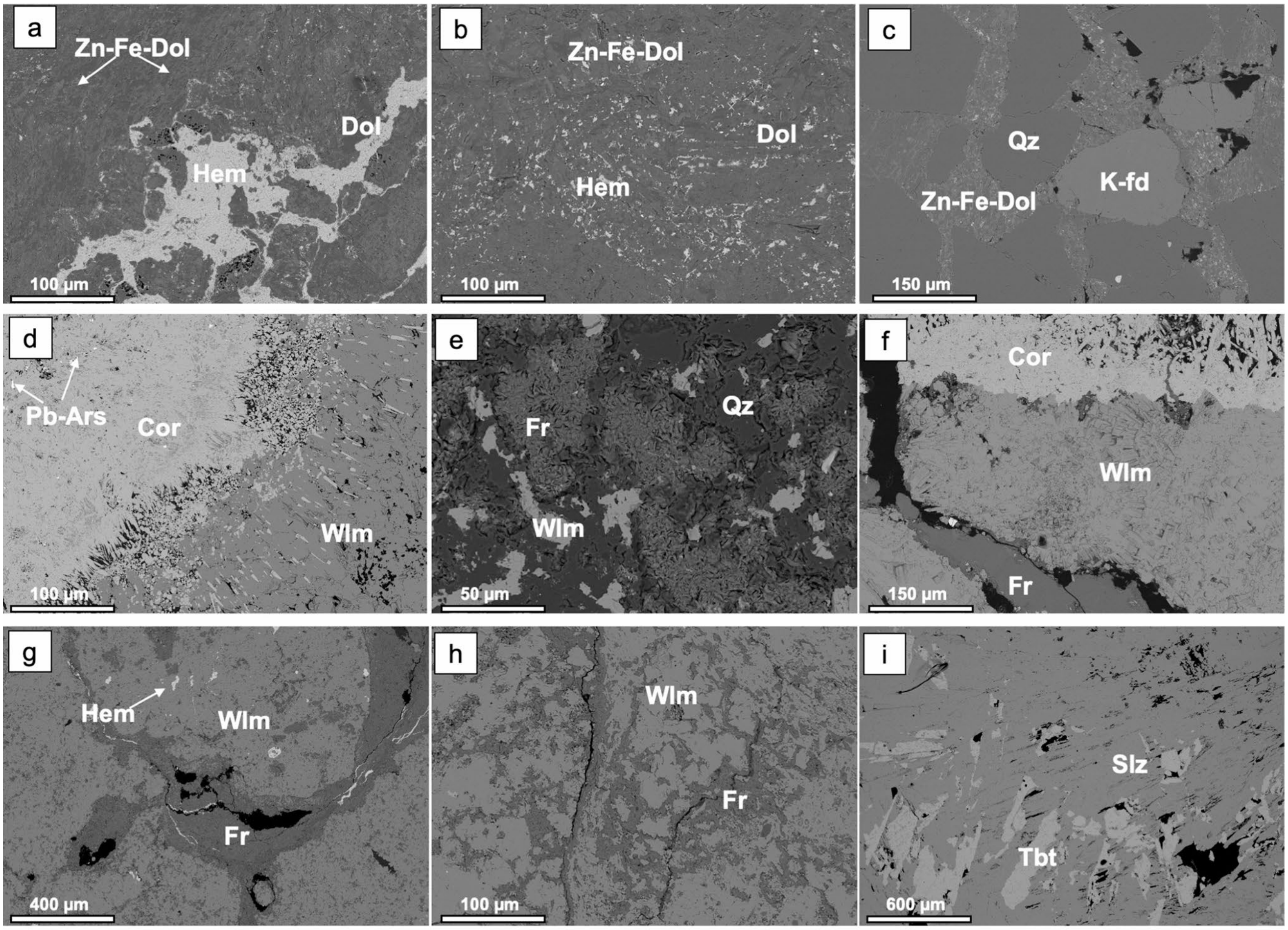

Fig. 3 FESEM-BSE textural images of the Beltana and Reaphook samples. **a** BE 3.04. Hematite vein in Zn-Fe-dolomite. **b** BE 3.04. Hematite disseminated in Zn-Fe-dolomite. **c** BE 2.04. Zn-Fe-dolomite cement in quartz arenite. **d** BE 7.04. Willemite and coronadite assemblage. **e** BE 7.04. Fraipontite and quartz cement in willemite. **f** BE 7.04A. Willemite and coronadite assemblage. **g** BE 1.04. Fraipontite vein in willemite. **h** BE 1.04. Fraipontite replacing early willemite. **i** RE 2.04. Scholtzite and tarbuttite assemblage. Ars: arsenate; Cor: coronadite; Dol: dolomite; Fr: fraipontite; Hem: hematite; K-fd: K-feldspar; Slz: scholzite; Tbt: tarbuttite; Wlm: willemite.

Table 2 Chemical compositions and stoichiometric formulas of selected fraipontite analyses obtained through FESEM-EDS

Sample	BE 7 04	BE 7 04A			BE 7 04b		BE 1.04													
	Site 6	Site 12			Site 1	Site 4	Site 1						Site 5			Site 6	Site 7	Site 8		
wt.%	**Spec 5**	**Spec 1**	**Spec 7**	**Spec 5**	**Spec 4**	**Spec 2**	**Spec 4**	**Spec 9**	**Spec 11**	**Spec 12**	**Spec 14**	**Spec 9**	**Spec 8**	**Spec 9**	**Spec 10**	**Spec 10**	**Spec 13**	**Spec 5**	**Spec 8**	**Spec 10**
SiO_2	27.55	24.26	26.95	24.86	23.27	26.72	24.56	24.59	25.30	24.19	24.89	24.88	24.84	24.97	24.23	24.46	24.25	24.86	23.87	24.89
TiO_2	0.02	0.05	0.05	0.00	0.00	0.00	0.10	0.25	0.08	0.06	0.00	0.00	0.04	0.53	0.08	0.00	0.00	0.05	0.00	0.00
Al_2O_3	16.84	14.64	16.47	17.74	19.38	15.00	16.12	14.18	14.52	14.54	14.77	15.95	15.35	14.67	15.78	15.45	15.76	16.04	16.00	16.08
FeO	0.95	8.04	1.65	1.24	0.42	1.05	0.69	3.30	1.57	3.17	1.79	1.24	1.40	2.63	1.92	2.40	1.57	1.24	1.38	0.97
MnO	0.09	0.41	0.30	0.16	0.13	0.19	0.13	0.22	0.09	0.13	0.14	0.26	0.09	0.03	0.13	0.05	0.03	0.08	0.05	0.00
MgO	12.28	6.80	6.94	6.72	3.00	13.81	3.90	4.89	5.27	3.85	4.35	4.78	4.72	5.23	3.99	4.11	3.75	4.54	3.59	4.03
CaO	0.37	0.25	0.31	0.12	0.40	1.30	0.08	0.11	0.17	0.10	0.14	0.17	0.15	0.13	0.04	0.07	0.08	0.06	0.18	0.03
K_2O	0.00	0.02	0.03	0.05	0.00	0.00	0.00	0.00	0.02	0.00	0.00	0.00	0.08	0.02	0.04	0.05	0.00	0.00	0.03	0.02
ZnO	30.65	35.22	36.55	39.37	41.20	30.61	44.16	42.06	43.01	43.55	44.62	43.30	42.18	42.40	42.78	43.19	44.12	42.36	43.11	44.54
H_2O+ = OH (stoich)	11.05	10.30	10.68	10.62	10.21	10.92	10.26	10.17	10.31	10.08	10.27	10.39	10.21	10.35	10.15	10.21	10.17	10.29	10.05	10.35
Total	99.80	99.99	99.93	100.88	98.01	99.60	100.00	99.77	100.34	99.67	100.97	100.97	99.06	100.96	99.14	99.99	99.73	99.52	98.26	100.91
atoms per formula unit (apfu) calculated on 14 negative charges $[O_5(OH)_4]$																				
Si	1.49	1.41	1.51	1.40	1.37	1.47	1.43	1.45	1.47	1.44	1.45	1.44	1.46	1.45	1.43	1.44	1.43	1.45	1.42	1.44
Al	0.51	0.59	0.49	0.60	0.63	0.53	0.57	0.55	0.53	0.56	0.55	0.56	0.54	0.55	0.57	0.56	0.57	0.55	0.58	0.56
sum tetr	2.00	2.00	2.00	2.00	2.00	2.00	2.00	2.00	2.00	2.00	2.00	2.00	2.00	2.00	2.00	2.00	2.00	2.00	2.00	2.00
Al	0.57	0.42	0.60	0.58	0.71	0.44	0.54	0.43	0.47	0.46	0.47	0.52	0.52	0.45	0.53	0.50	0.52	0.55	0.55	0.54
Ti	0.00	0.00	0.00	0.00	0.00	0.00	0.00	0.01	0.00	0.00	0.00	0.00	0.00	0.02	0.00	0.00	0.00	0.00	0.00	0.00
Fe^{2+}	0.04	0.39	0.08	0.06	0.02	0.05	0.03	0.16	0.08	0.16	0.09	0.06	0.07	0.13	0.09	0.12	0.08	0.06	0.07	0.05
Mn	0.00	0.02	0.01	0.01	0.01	0.01	0.01	0.01	0.00	0.01	0.01	0.01	0.00	0.00	0.01	0.00	0.00	0.00	0.00	0.00
Mg	0.99	0.59	0.58	0.56	0.26	1.13	0.34	0.43	0.46	0.34	0.38	0.41	0.41	0.45	0.35	0.36	0.33	0.39	0.32	0.35
Zn	1.34	1.65	1.65	1.79	1.94	1.35	2.07	1.99	2.01	2.08	2.09	2.01	1.99	1.97	2.03	2.04	2.09	1.99	2.07	2.07
sum oct	2.95	3.07	2.92	3.00	2.94	2.97	3.00	3.04	3.02	3.04	3.03	3.01	3.00	3.02	3.01	3.02	3.02	3.00	3.00	3.01
Ca	0.02	0.02	0.02	0.01	0.03	0.08	0.01	0.01	0.01	0.01	0.01	0.01	0.01	0.01	0.00	0.00	0.01	0.00	0.01	0.00
K	0.00	0.00	0.00	0.00	0.00	0.00	0.00	0.00	0.00	0.00	0.00	0.00	0.01	0.00	0.00	0.00	0.00	0.00	0.00	0.00
sum major cations	0.02	0.02	0.02	0.01	0.03	0.08	0.01	0.01	0.01	0.01	0.01	0.01	0.02	0.01	0.01	0.01	0.01	0.00	0.01	0.00

Table 2 (continued)

Sample	BE 1.04						BE 1.04 PIT						BE 5.04(1)			
	Site 9			Site 11	Site 12		Site 2		Site 5			Site 6	Site 3	Site 5	Site 7	
wt.%	**Spec 6**	**Spec 7**	**Spec 8**	**Spec 5**	**Spec 1**	**Spec 4**	**Spec 6**	**Spec 5**	**Spec 6**	**Spec 2**	**Spec 3**	**Spec 3**	**Spec 7**	**Spec 2**	**Spec 4**	**Spec 11**
SiO_2	24.17	23.22	24.88	24.54	24.90	25.27	25.34	25.58	24.89	25.43	24.45	25.08	27.89	23.77	25.73	25.92
TiO_2	0.09	0.22	0.06	0.04	0.03	0.00	0.00	0.00	0.29	0.05	0.17	0.29	0.00	0.00	0.01	0.04
Al_2O_3	15.03	15.33	14.96	16.38	16.16	15.96	14.92	16.05	14.14	14.87	15.25	14.71	15.26	19.62	15.39	15.81
FeO	3.23	2.51	1.03	0.94	0.58	0.91	0.86	0.98	3.72	3.42	2.31	1.65	2.85	0.59	1.74	0.78
MnO	0.14	0.00	0.03	0.10	0.00	0.00	0.24	0.00	0.06	0.10	0.15	0.26	0.17	0.13	0.13	0.12
MgO	4.72	3.78	4.78	3.94	4.28	4.99	5.09	5.17	6.07	5.72	4.28	5.22	10.65	5.82	9.27	8.65
CaO	0.11	0.13	0.21	0.17	0.10	0.12	0.12	0.14	0.11	0.12	0.09	0.19	0.08	0.11	0.24	0.18
K_2O	0.00	0.03	0.02	0.00	0.00	0.00	0.00	0.00	0.02	0.00	0.00	0.00	0.09	0.00	0.00	0.01
ZnO	42.01	42.31	42.90	43.24	44.14	42.92	42.02	42.59	40.15	40.74	43.88	41.46	32.43	38.99	36.41	37.84
H_2O+ = OH (stoich)	10.17	9.91	10.19	10.26	10.35	10.41	10.23	10.48	10.26	10.41	10.27	10.23	10.90	10.53	10.58	10.63
Total	99.67	97.44	99.06	99.61	1100.54	100.58	98.82	100.99	99.71	100.86	100.85	99.09	100.32	99.56	99.50	99.98
atoms per formula unit (apfu) calculated on 14 negative charges $[O_5(OH)_4]$																
Si	1.42	1.40	1.46	1.43	1.44	1.45	1.48	1.46	1.45	1.46	1.43	1.47	1.53	1.35	1.46	1.46
Al	0.58	0.60	0.54	0.57	0.56	0.55	0.52	0.54	0.55	0.54	0.57	0.53	0.47	0.65	0.54	0.54
sum tetr	2.00	2.00	2.00	2.00	2.00	2.00	2.00	2.00	2.00	2.00	2.00	2.00	2.00	2.00	2.00	2.00
Al	0.47	0.50	0.50	0.56	0.54	0.54	0.51	0.54	0.43	0.47	0.48	0.48	0.52	0.67	0.48	0.51
Ti	0.00	0.01	0.00	0.00	0.00	0.00	0.00	0.00	0.01	0.00	0.01	0.01	0.00	0.00	0.00	0.00
Fe^{2+}	0.16	0.13	0.05	0.05	0.03	0.04	0.04	0.05	0.18	0.16	0.11	0.08	0.13	0.03	0.08	0.04
Mn	0.01	0.00	0.00	0.00	0.00	0.00	0.01	0.00	0.00	0.00	0.01	0.01	0.01	0.01	0.01	0.01
Mg	0.41	0.34	0.42	0.34	0.37	0.43	0.44	0.44	0.53	0.49	0.37	0.46	0.87	0.49	0.78	0.73
Zn	1.99	2.06	2.03	2.03	2.06	1.99	1.98	1.96	1.89	1.89	2.06	1.95	1.43	1.79	1.66	1.72
sum oct	3.04	3.03	3.00	2.99	3.00	3.00	2.99	2.99	3.04	3.02	3.04	3.00	2.97	2.98	3.01	3.00
Ca	0.01	0.01	0.01	0.01	0.01	0.01	0.01	0.01	0.01	0.01	0.01	0.01	0.00	0.01	0.01	0.01
K	0.00	0.00	0.00	0.00	0.00	0.00	0.00	0.00	0.00	0.00	0.00	0.00	0.01	0.00	0.00	0.00
sum major cations	0.01	0.01	0.01	0.01	0.01	0.01	0.01	0.01	0.01	0.01	0.01	0.01	0.01	0.01	0.01	0.01

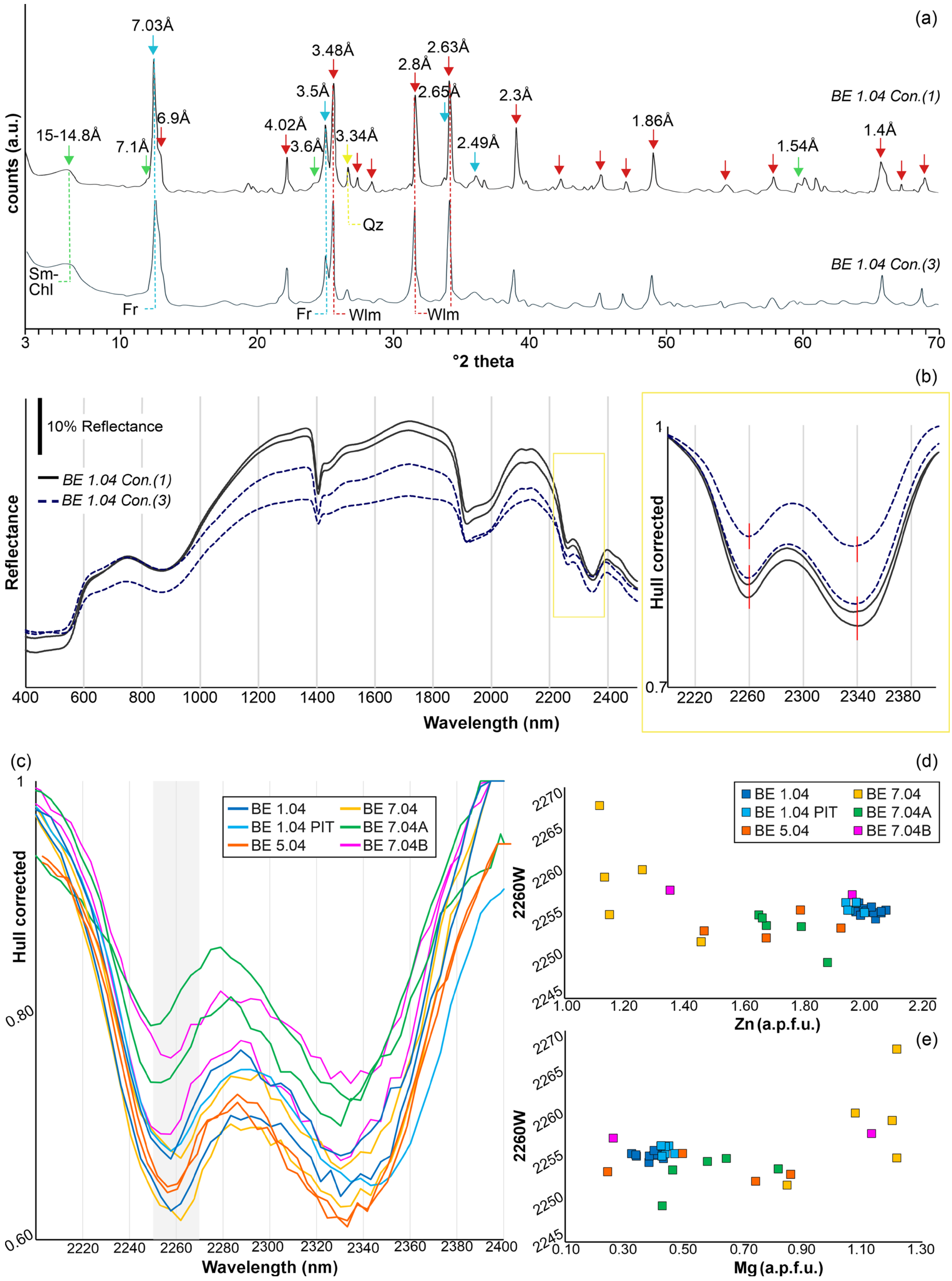
(a)
counts (a.u.)
7.03Å
3.48Å
2.63Å
2.8Å
3.5Å
2.65Å
2.3Å
6.9Å
15-14.8Å
7.1Å
4.02Å
3.6Å
3.34Å
2.49Å
1.86Å
1.4Å
1.54Å
BE 1.04 Con.(1)
BE 1.04 Con.(3)
Qz
Sm-Chl
Fr
Fr
Wlm
Wlm
3
10
20
30
40
50
60
70
°2 theta
(b)
10% Reflectance
BE 1.04 Con.(1)
BE 1.04 Con.(3)
Reflectance
400
600
800
1000
1200
1400
1600
1800
2000
2200
2400
Wavelength (nm)
Hull corrected
1
0.7
2220
2260
2300
2340
2380
(c)
Hull corrected
1
0.80
0.60
BE 1.04
BE 1.04 PIT
BE 5.04
BE 7.04
BE 7.04A
BE 7.04B
2220
2240
2260
2280
2300
2320
2340
2360
2380
2400
Wavelength (nm)
(d)
BE 1.04
BE 1.04 PIT
BE 5.04
BE 7.04
BE 7.04A
BE 7.04B
2260W
2270
2265
2260
2255
2250
2245
1.00
1.20
1.40
1.60
1.80
2.00
2.20
Zn (a.p.f.u.)
(e)
2260W
2270
2265
2260
2255
2250
2245
0.10
0.30
0.50
0.70
0.90
1.10
1.30
Mg (a.p.f.u.)

◀ **Fig. 4** **a** XRPD results of two fraipontite concentrates from the mineralized BE 1.04 sample. **b** two ASD FieldSpec-4 spectrometer reflectance spectra for each concentrated mineral phase. **c** enlargement of the 2200–2400 nm spectral range, showing the shift in the wavelength position of the 2260 nm absorption feature of fraipontite in all the mineralized samples, derived from the hyperspectral scans, along with scatter plots between 2260W and content of major Zn and Mg cations in the octahedral site. Chl: chlorite; Fr: fraipontite; Qz: quartz; Sm: smectites; Wlm: willemite

comparatively lower Zn contents (down to 30 wt% ZnO) and higher MgO values (up to 13.8 wt% MgO) (Table 2).

Sample BE 4.04 is mainly composed of arsenates, mostly hedyphane and mimetite, occurring as vug fillings within a matrix of coronadite with minor clay phases containing ~ 2 wt% Zn, crosscut by calcite veins (see Table A2 in the ESM). The two samples (RE 1.04 and RE 2.04) from the Reaphook Hill area are composed almost entirely of Zn-bearing phosphates, in association with minor Fe and Mn oxy-hydroxides, quartz, and phyllosilicates. Sample RE 1.04 predominantly contains scholzite that occurs within voids as radial aggregates of white to colorless prismatic needles (Fig. 3i), along with lesser quantities of Fe- and Mn-oxy-hydroxides and apatite (see Table A2). Sample RE 2.04 contains the same mineral phases, with higher abundances of tarbuttite, which appears as compact aggregates of crystals with an equant to prismatic habit, along with minor amounts of fraipontite (see Table A2).

Reflectance spectroscopy of ground samples

Beltana mining area - The ASD spectra of the host dolomite breccia (*S1* and *S2* in Fig. 5c; sample BE 3.04) show a pronounced carbonate absorption at 2322 nm with an asymmetric shoulder at 2272 nm, indicating the presence of Fe-dolomite. The absorptions observed at 890, 540, and 650 nm are diagnostic of hematite (Hunt 1977; Burns 1993; Crowley et al. 2003). The *S3* spectrum from the host quartzite (sample BE 2.04 in Fig. 5f) exhibits shallow Al-OH absorptions at around 1400, 2200, and 2343 nm arising from muscovite presence (Velde 1965; Laukamp et al. 2021). The *S4* spectrum, acquired from the red spots (Fig. 5d) with characteristic absorptions at 890 and 2322 nm, highlights the occurrence of hematite and Fe-bearing dolomite in the sample (Fig. 5f;Gaffey 1986; Van Der Meer 1995; Lampinen et al. 2019).

In the mineralized samples, willemite was spectrally inactive (as also reported by McConachy et al. 2007). However, in correspondence with the red willemite only, the spectra (i.e., *S5* and *S6* spectra in Fig. 5i) display an absorption feature at ~ 900 nm, likely attributable to hematite either as inclusions in the mineral or as void fillings. This spectral signature enables the mapping of the red willemite and hematite association, as it disappears in the white willemite (i.e., spectra *S7* and *S8* in Fig. 5i). The reflectance spectrum of fraipontite, acquired for the first time in the current study, was characterized by absorption features at ~ 1400 nm and at ~2260 nm (between 2250 and 2265 nm) (Fig. 4b and c and spectra *S5* to *S8* in Fig. 5i). The correspondence between spectral features and mineral chemical composition was traced through the comparison of point spectral analyses, hyperspectral sample maps, and FESEM-EDS images (Fig. 4d and e). The shift in the absorption feature from shorter (~2250 nm) to longer (~2265 nm) wavelengths seems to be locally associated with the increase in Mg contents in the Zn-clay (Fig. 4c). Fraipontite in hyperspectral sample images was thus mapped by fitting a quadratic polynomial between 2250 and 2280 nm (Table 1). Fraipontite represents the most abundant spectrally active zinc mineral in the system besides the Zn-carbonates, identified by a minimum wavelength at ~ 2360 nm for smithsonite (see spectra *S7* and *S8* in Fig. 5i).

The arsenate mineral group was identified based on double absorptions at ~ 1437 and ~ 1940 nm, related to the overlap of OH/H_2O vibrational modes (*S9* and *S10* spectra in Fig. 5n). Nevertheless, it was challenging to discriminate between hedyphane and mimetite, as their main spectral absorption features are identical. Coronadite is a dark Pb oxide and, therefore, lacks a diagnostic feature with only a weak absorption at 2210 nm (due to Al-OH and/or Zn-OH bonding), likely arising from smectites disseminated in the matrix (spectra *S11* in Fig. 5n). Finally, the feature at 2336 nm enabled the identification of late calcite veins (spectra *S9* in Fig. 5n).

Reaphook area - The spectra of the samples RE 1.04 and RE 2.04 (i.e., *S12* to *S15* in Fig. 6c) show a broad Fe absorption centered at ~ 950 nm related to goethite (*S13* to *S15*), combined with absorption features at 2260 nm due to fraipontite (*S14* and *S15*) and well-developed features between 1400 and 1700 nm and 2300–2400 nm associated with the Zn-phosphates (as also reported by McConachy et al. 2007). Specifically, the Zn-OH bending modes generate spectral absorptions at ~ 2430 nm for scholzite, and double reflectance peaks towards shorter wavelengths at 2310 and 2370 nm for tarbuttite. Additional combination tones of water (H_2O) and hydroxyl (OH) groups occur at around 1480, 1590, 1760, and 1960 nm, for scholzite, with a shift to 1495, 1730, and 1950 nm for tarbuttite (spectra *S12* to *S15*).

EnMAP-derived mineral maps

Beltana mining area

The spectral analysis of the Beltana mining area (Fig. 7a) reveals that the majority (> 50%) of the exposed rocks are carbonates (2330D), in agreement with the geological

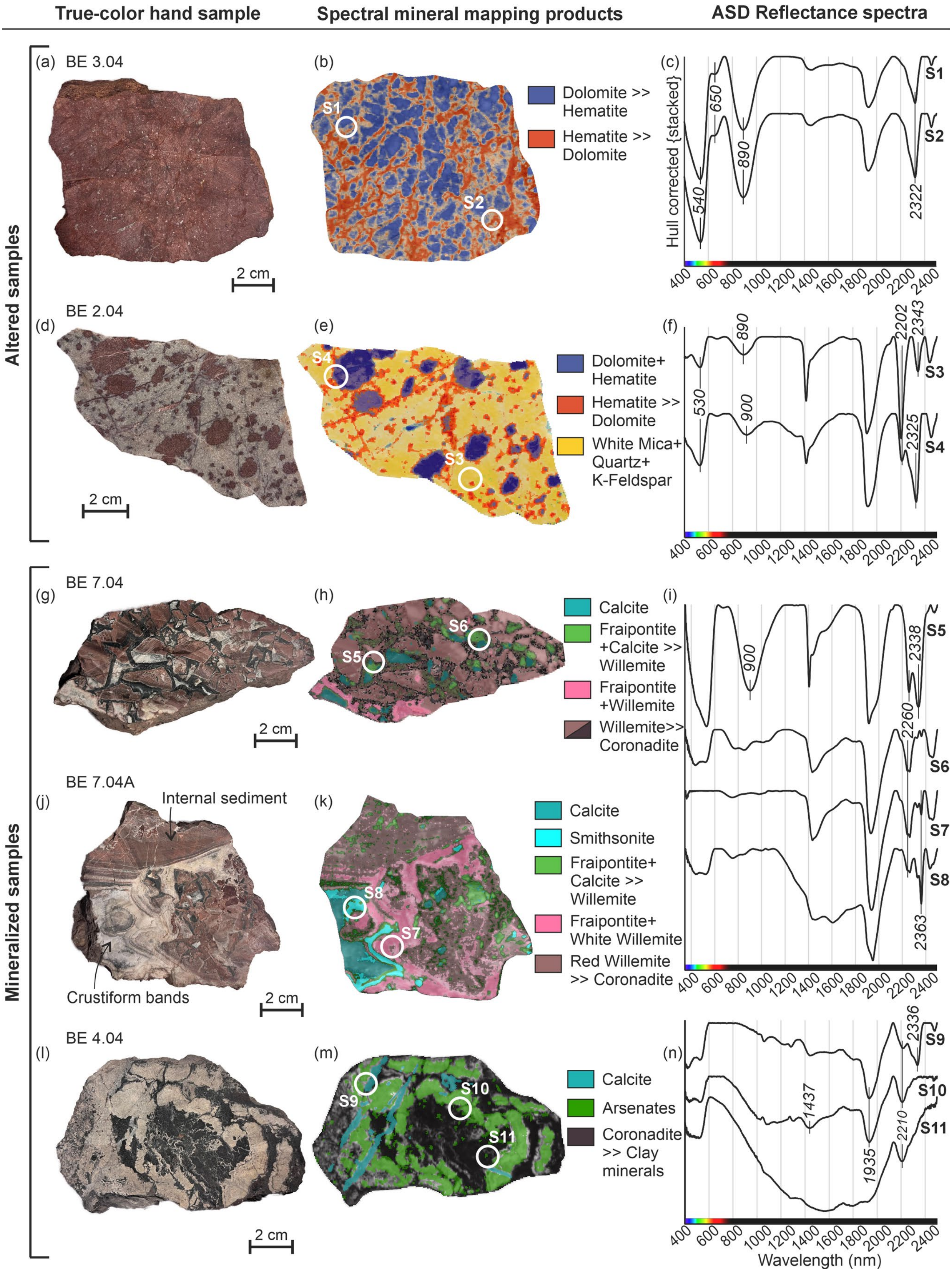
True-color hand sample
Spectral mineral mapping products
ASD Reflectance spectra
Altered samples
(a) BE 3.04
2 cm
(b)
S1
S2
Dolomite >> Hematite
Hematite >> Dolomite
(c)
Hull corrected {stacked}
650
890
540
2322
S1
S2
400 600 800 1000 1200 1400 1600 1800 2000 2200 2400
BE 2.04
(d)
2 cm
(e)
S4
S3
Dolomite+ Hematite
Hematite >> Dolomite
White Mica+ Quartz+ K-Feldspar
(f)
890
2202
2343
530
900
2325
S3
S4
400 600 800 1000 1200 1400 1600 1800 2000 2200 2400
Mineralized samples
BE 7.04
(g)
2 cm
(h)
S5
S6
Calcite
Fraipontite +Calcite >> Willemite
Fraipontite +Willemite
Willemite>> Coronadite
(i)
900
2338
2260
2363
S5
S6
S7
S8
BE 7.04A
(j)
Internal sediment
Crustiform bands
2 cm
(k)
S8
S7
Calcite
Smithsonite
Fraipontite+ Calcite >> Willemite
Fraipontite+ White Willemite
Red Willemite >> Coronadite
400 600 800 1000 1200 1400 1600 1800 2000 2200 2400
BE 4.04
(l)
2 cm
(m)
S9
S10
S11
Calcite
Arsenates
Coronadite >> Clay minerals
(n)
2336
1437
1935
2210
S9
S10
S11
400 600 800 1000 1200 1400 1600 1800 2000 2200 2400
Wavelength (nm)

Fig. 5 Hyperspectral scans of selected altered and mineralized hand samples from Beltana. **a**, **d**, **g**, **j**, **l** show the true-color composite imagery. **b**, **e**, **h**, **k**, **m** show the spectrally mapped minerals. White circles mark the ASD measure points, the circle size indicates the contact probe window diameter. **c**, **f**, **i**, **n** Hull-corrected reflectance spectra with the major absorption features noted

map (Fig. 2a). The map of minimum wavelength position (2330W; Fig. 7c) shows variations between 2305 and 2350 nm, enabling the discrimination between dolomite (blue-cyan) and calcite (yellow-red), corresponding to a shift from ~2314–2322 nm to ~2337–2340 nm. The relative abundance map of iron oxides/hydroxides (Fig. 7d) exhibits the highest values towards the eastern end. The main absorption feature shifts toward the shorter wavelengths (900W; Fig. 7e), from goethite (blue to green) to hematite (yellow to red), especially at mineralized zones. Based on the spectral features identified in the mineralized samples (e.g., samples BE 7.04 and BE7.04 A in Fig. 5), the fraipontite absorption feature centered at ~2260 nm was mapped with the deepest absorptions (orange to red) located near the Beltana open-pit. Other scattered occurrences with medium to high relative abundances are found at Sundown and Wallrider. The relative abundances of white mica and kaolinite (Fig. 7g and i) appear to be correlated with outcropping sandstones. These units are characterized by Al-rich white mica (blue to green in Fig. 7h), with the Al-OH absorption varying between 2190 and 2207 nm. The basal volcanic rocks of the Callanna Group, exposed to the south-west, are typified by Al-poor compositions, marked by an Al-OH absorption between 2210 and 2216 nm (red colors in Fig. 7h). Kaolinite is primarily mapped over quartzites and sandstones in the area (Fig. 7i).

Beltana – Aroona trend

A broader view of the mineral maps encompassing the entire Beltana – Aroona mineralized district (Fig. 8a) confirm the maxima of kaolinite and white mica features (Fig. 8b) in correspondence of the exposed quartzites and sandstones (Fig. 2a). The highest carbonate relative abundances (Fig. 8c) are observed instead in correspondence of outcrops along the NW-SE direction, corresponding to Wonoka, Ajax, and Aroona Creek Formations (Fig. 2a). The dolomite-rich zones are mostly distributed across the Ajax Limestone Formation, at the Aroona prospects, and are also common in the southernmost exposure of this formation, in correspondence with Mount Scott occurrences, extending along strike, until the North Moolooloo deposit (Fig. 8d). The Fe oxy-hydroxides map (Fig. 8e) reveals that the goethite feature (blue to green) is widespread in the area, whereas hematite, depicted in red hues, occurs in scattered patches only in the known ore zones. The 2260 nm fraipontite absorption feature was mapped with the deepest feature in the Aroona prospect (Fig. 8f). In contrast, the occurrences of this feature observed further south (Fig. 8f), are associated with shifts at ~2250–2257 nm, likely indicating an absorption overlap with Fe-rich chlorites.

Reaphook area

The carbonate relative abundance map (Fig. 9b) of the Reaphook area (Fig. 9a) reveals that this mineral group is common. Overall, dolomite forms broad haloes around all the mineralized occurrences at Reaphook, Reaphook Hill, and finally, at Reaphook North at the contact with quartzites and sandstones (Fig. 9c). Despite the striping noise in the 900 nm region, Fe oxy-hydroxides were detected in the area (Fig. 9d), with the goethite-hematite ratio map (Fig. 9e) showing the dominance of the goethite feature over hematite. The deepest features of hematite and fraipontite are restricted to smaller outcrops, occurring as elongated bodies such as the one just north of Reaphook Hill, and as clusters, like those to the north-west of Reaphook Hill and north of the Reaphook North occurrences (Fig. 9e and f). As for other areas, the map of Al-sheet silicates, including white mica and kaolinite (Fig. 9g and i), shows high abundances in the outcropping quartzites, sandstones, and siltstones.

Multivariate statistical analysis of the EenMAPmap spectral data and lithofacies prediction via machine learning algorithms

The principal component analysis conducted on the EnMAP data of the Beltana – Aroona district, revealed the statistical relationships between the mapped minerals. In the first PCA on 5 variables (i.e., the spectral features 2200D, 2165D, 2330D, 900D, and 2260D), 90% of the variance is explained by the first three components (PC1 = 45.64%, PC2 = 25.11% and PC3 = 17.18%; see Fig. A1 in the ESM). PC1 explains the positive correlation between white mica and kaolinite, whereas PC2 is mostly controlled by the association of fraipontite + carbonates (negative PC2 scores; Fig. A1). PC3 is controlled by the spectral features of Fe-oxy-hydroxides (see Fig. A1). The maps of the PCn scores relate to the outcropping geology, with the PC1 positive scores associated with the siliciclastic lithologies, and the PC2 negative scores mainly to the mineralized areas (see Fig. A2). The PCA conducted on the modified database comprising 7 variables (i.e., dolomite, calcite, hematite, goethite, fraipontite, white mica and kaolinite) had the first three components explaining 77% of the total variance (PC1 = 38.16%, PC2 = 22.86% and PC3 = 15.51%; Fig. A1). PC1 and PC2 control the

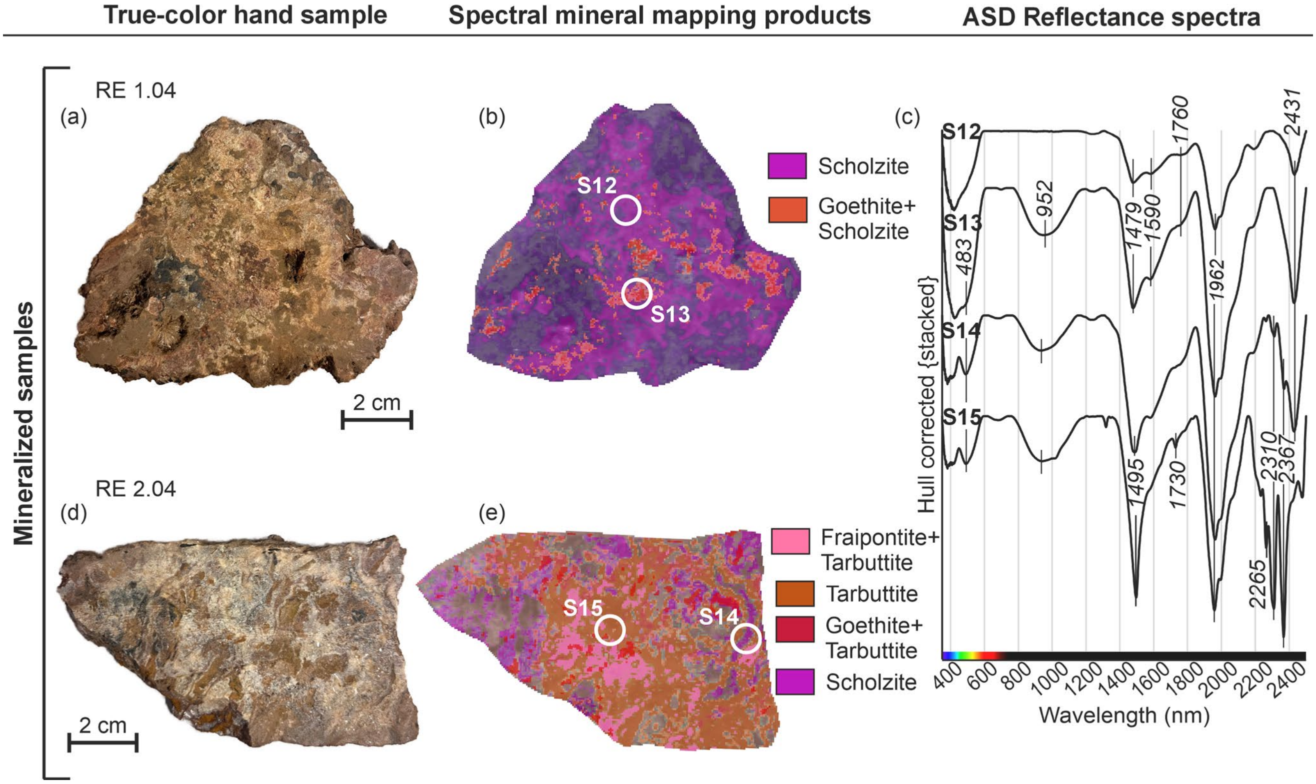

Fig. 6 Hyperspectral scans of selected mineralized hand samples from Reaphook. **a**, **d** show the true-color composite imagery. **b**, **e** show the spectrally mapped minerals. White circles mark the ASD measure points, the circle size indicates the contact probe window diameter. **c** Hull-corrected reflectance spectra with the major absorption features noted

first-order correlation between dolomite + calcite, hematite + goethite and white mica + kaolinite, whereas PC3 describes the correlation between dolomite and fraipontite (see Figs. A1 and A2); the maximum PC3 scores are indicative of the mineralized areas (see Figs. A1 and A2). This correlation between dolomite and fraipontite, together with hematite – i.e., the spectrally active minerals of the ore mineral association – is also evident when plotting the co-occurrence of these three mineral phases (Fig. 10a). In fact, it appears that their mineral features occur all together in very limited areas of the map, precisely corresponding to the mineralized sites (Fig. 2a).

The machine learning algorithm was performed on the relative abundances of dolomite, calcite, hematite, goethite, fraipontite, white mica, and kaolinite, obtained from the EnMAP data and used for the second PCA. The optimization process via cross-validation produced 100 XGBoost algorithms having very high accuracy scores for both the training (mean accuracy: 0.9991, σ: 0.0018) and the testing dataset (mean accuracy: 0.9767, σ: 0.0076). The comparison between the predicted lithofacies map with the geological formations (Figs. 2a and 10b) shows a match of more than 80% (Table 3). For example, the Ajax Limestone Formation, which hosts the mineralization, gives a total correspondence of ~ 82% with carbonate signatures, distributed as 13% limestone, 29% carbonate cover, and 40% dolomitization (Table 3). In the case of formations consisting of mixed lithologies, the correspondence is lower. The predicted lithofacies "Mineralized zones" (defined by dolomite + hematite + fraipontite spectral signatures) reaches the highest match with the "mineralized sites" of the geological map (11%), lower correspondences with the Ajax Limestone (1.3%), and with all the other mapped formations (< 0.2% correspondence).

Discussion

Detection of hydrothermal alteration and ore minerals from satellite spectral data

From the literature, the occurrences of Zn mineralization in the study areas are structurally-controlled and associated with pervasive hydrothermal alteration, which is characterized by hematite and dolomite (Groves et al. 2003). Mineralogical analyses and laboratory hyperspectral investigations of hand samples allowed the identification of previously documented Zn-minerals and provided new insights into their spectral behavior. The main ore mineral,

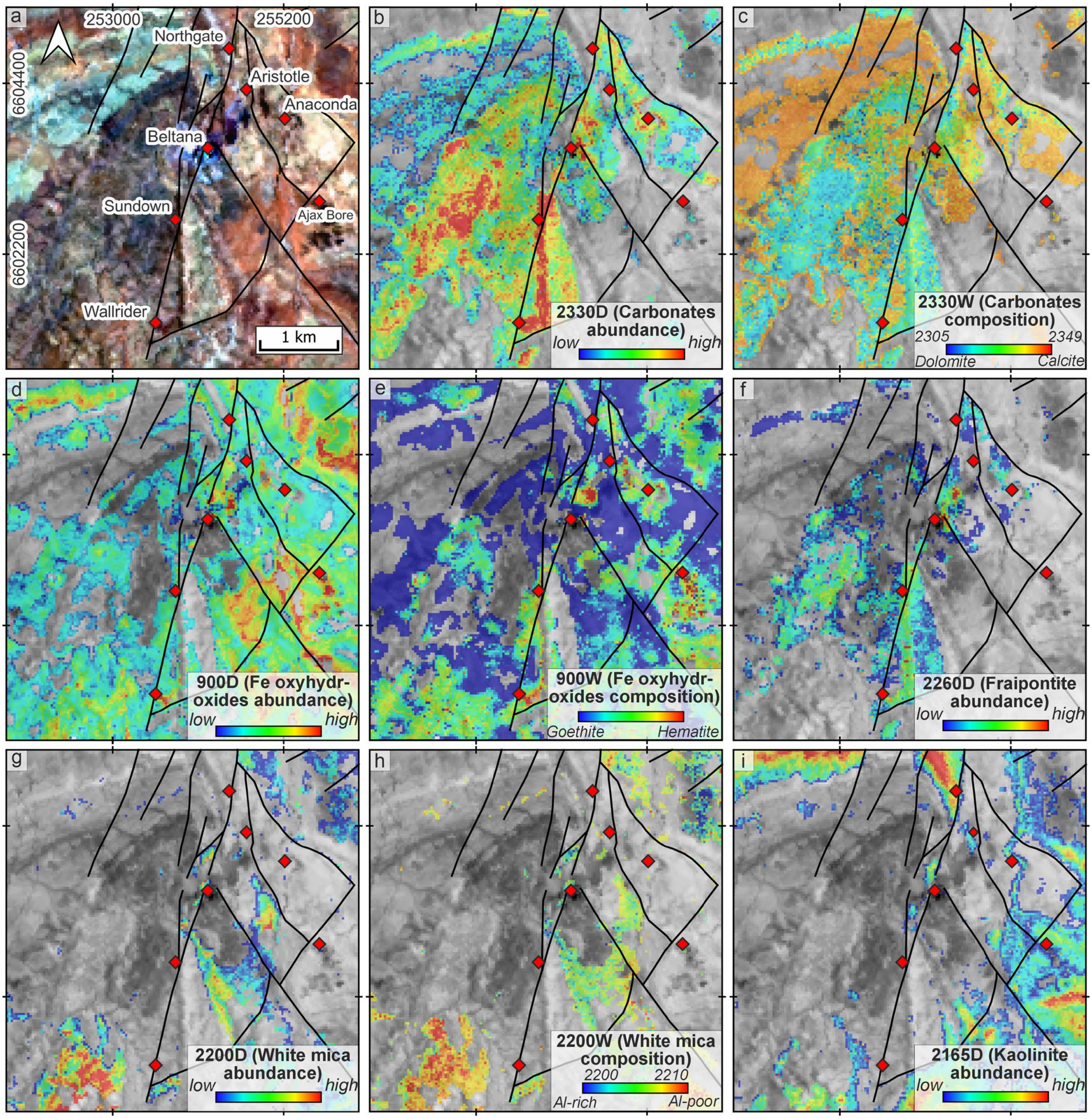

Fig. 7 Mineral mapping products derived from EnMAP hyperspectral data over the Beltana mining area. **a** True-color composite image with the location of known mineral deposits (red diamonds). **b** Carbonates relative abundance map (2330D). **c** Carbonate mineralogy showing variations in the minimum wavelength of 2330 nm (2330W) with calcite and dolomite at two ends. **d** Ferric iron relative abundance map (900D). **e** Ferric iron composition map (900W). **f** 2260 nm feature depth map (2260D). **g** White mica relative abundance map (2200D). **h** White mica mineralogic map (2200W) with Al-poor and Al-rich at two ends. **i** Kaolinite relative abundance map (2165D). The color-coded mineral maps are superimposed on the albedo image of the area. Solid black lines depict the faults (from Groves et al. 2003)

willemite, in the Beltana-Aroona samples is not spectrally active in the VNIR-SWIR range and cannot be mapped in the satellite images (McConachy et al. 2007). Smithsonite has very low concentrations and has spectral features in part overlapped with secondary absorptions of Al-sheet silicates. Similarly, although scholzite and tarbuttite were detected in hand samples from Reaphook Hill, their detection at the 30 m pixel size of EnMAP was very challenging. This is because the main absorption feature of scholzite is located beyond the 2400 nm wavelength in a highly noisy region,

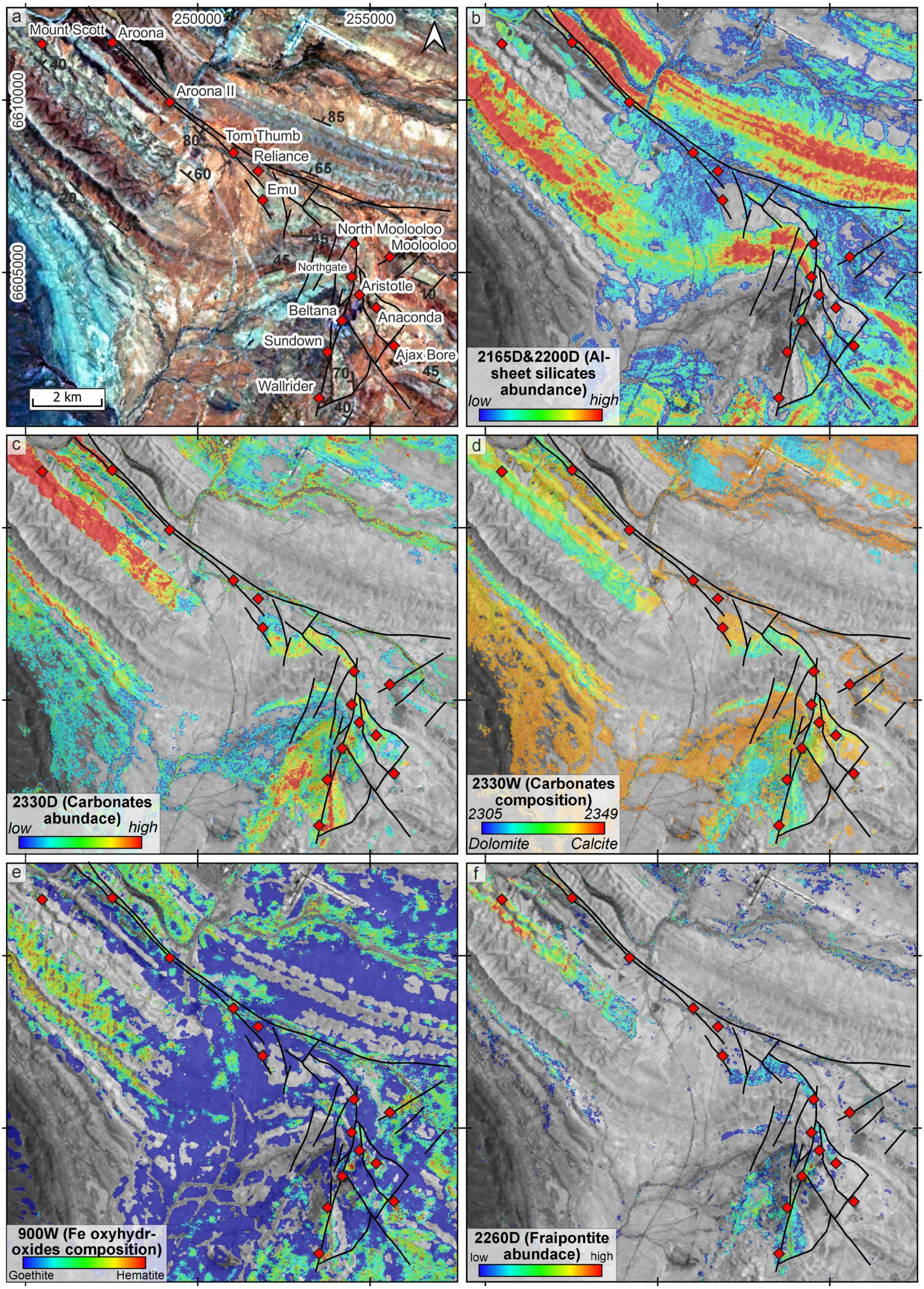
a
250000
255000
6610000
6605000
Mount Scott
Aroona
Aroona II
Tom Thumb
Reliance
Emu
North Moolooloo
Moolooloo
Northgate
Aristotle
Beltana
Anaconda
Sundown
Ajax Bore
Wallrider
40
85
80
60
65
20
35
45
45
10
70
45
40
2 km
b
2165D&2200D (Al-sheet silicates abundance)
low
high
c
2330D (Carbonates abundace)
low
high
d
2330W (Carbonates composition)
2305
2349
Dolomite
Calcite
e
900W (Fe oxyhydr-oxides composition)
Goethite
Hematite
f
2260D (Fraipontite abudace)
low
high

Fig. 8 Mineral mapping products derived from EnMAP hyperspectral data over the Beltana-Aroona areas. **a** True-color composite image with the location of known mineral deposits (red diamonds). **b** White mica and kaolinite relative abundance map (2165D&2200D). **c** Carbonates relative abundance map (2330D). **d** Carbonates mineralogy showing variations in the minimum wavelength of 2330 nm (2330W) with calcite and dolomite at two ends. **e** Ferric iron composition map (900W). **f** 2260 nm feature depth map (2260D). The color-coded mineral maps are superimposed on the albedo image of the area. Solid black lines depict the faults (from Groves et al. 2003)

whereas the double absorption feature of tarbuttite overlaps with carbonate signatures (at ~2310 and 2370 nm). Therefore, to map the mineralized rocks in both study areas, we investigated the spectral behavior of fraipontite, which to our knowledge, has never been reported in the literature on these deposits.

The occurrence of fraipontite in the ore samples was first confirmed with XRPD patterns and FESEM-EDS analyses, obtained on the clay-rich matrix (Fig. 4a; Table 2). The chemical formulas in *atoms per formula unit* (*apfu*) of these Zn-clays were calculated following the stoichiometry by Newman and Brown (1987), by using 14 negative charges $[O_5(OH)_4]$ as for the 1:1 species (i.e., kaolinite-serpentine group). Iron was considered bivalent as in trioctahedral clays (Fe^{2+}). The resulting average chemical formula $(Zn_{1.91}, Al_{0.52}, Mg_{0.48}, Fe^{2+}{}_{0.09})(Si_{1.45},Al_{0.55})O_5(OH)_4$ (Table 2), confirms the fraipontite nature of these Zn-clays. The positive correlation between Zn vs. Mg *apfu* ($R^2 = 0.90$) possibly indicates a Zn-Mg substitution in the octahedral site (Table 2). In several EDS analyses characterized by low-quality stoichiometry, a subtle correlation between Mg and Ca could indicate the presence of Mg-smectite traces, as also observed in the XRPD patterns.

The association of willemite and fraipontite is not new in the literature; it has been detected in the La Calamine mine, Belgium (Coppola et al. 2008), Bou Arhous, Marocco (Choulet et al. 2016), and Kihabe, Namibia (Putzolu et al. 2023). In the Kihabe deposit (Putzolu et al. 2023), through the use of XRPD analyses on clay separates and High Resolution Transmission Electron Microscopy investigations (HRTEM), it was documented the intimate association between fraipontite and smectite. Putzolu et al. (2023) highlighted the difficulties in distinguishing between these phases and baileychlore, a 14 Å-type 2:1:1 trioctahedral mineral, the Zn-rich end-member of the chlorite group. Although in this study we did not perform specific analyses on oriented clay aggregates, we are certain our samples contain fraipontite + minor Mg-smectite, and not baileychlore or even sauconite, for the following reasons: (1) the 14.8–15 Å peak occurring in the bulk XRDP patterns is very broad, in contrast to the 7 Å peak that is more sharp – this suggests two distinct phases: a 15 Å-type 2:1 clay and a 7 Å-type 1:1 clay, not a single 14 Å-type 2:1:1 phase (e.g. baileychlore); (2) the EDS analyses and ASD spectra of the Zn-clays do not match the stoichiometry and structure of sauconite (McConachy et al. 2007); (3) no other EDS analyses besides those of the Zn-clays could be turned into a 7 Å phyllosilicate to explain the XRPD data.

The newly identified spectral features of fraipontite at ~1400 nm and ~2260 nm would be likely attributable, respectively, to the OH-bond vibrations and to the vibrational modes of Zn-OH bonds in this Zn-clay, similarly to other phyllosilicates (Fig. 4b and c, and spectra *S5* to *S8* in Fig. 5i; Laukamp et al. 2021). In the sample BE 1.04, where fraipontite exhibits a coherent composition around Zn 2.00 apfu, Al 0.60 apfu, and Mg 0.50 apfu, the point spectra obtained from the HySpec imaging system gave a wavelength absorption between 2257 and 2260 nm (Fig. 4b, c, d and e). In a few anomalous samples (BE 7.04 and BE 7.04B), the 2260 nm absorption feature was observed to shift toward longer wavelengths (~2265 nm; Fig. 4e), in association with the local increase in the Mg contents in the Zn-clay (Fig. 4d and e). Consequently, the feature centered at 2260 nm in this context must be considered as diagnostic for fraipontite.

To assess the EnMAP capabilities, representative reflectance spectra were extracted from L2A EnMAP imagery covering the two test sites and compared to the resampled USGS spectral library (Kokaly et al. 2017) and spectral data collected using the ASD spectroradiometer (Fig. 11). Pixel spectra from the dolomitized alteration haloes (Fig. 11a) are characterized by the CO_3^{2-} absorption feature at ~2322 nm with a left-side shoulder centered at 2273 nm, which is identical to the spectrum *S1* and *S2* from the sample BE 3.04 in Fig. 5c, enabling the discrimination of Fe-dolomite from calcite (Fig. 11a). The broad absorption features of hematite at ~870 nm and goethite at ~940 nm (Fig. 11b) are also comparable to image pixels, despite the intrinsic noise of the instrument in this range. But upon spectral smoothing (orange line), they appear to be similar to the USGS reference spectra. The EnMAP spectrum shown in Fig. 11c was extracted from a pixel corresponding to a mineralized zone and is characterized by the association of dolomite (2322 nm) and fraipontite (2257 nm). As the fraipontite spectrum is not yet available in the existing literature (e.g., McConachy et al. 2007), the EnMAP spectral signature was compared against the Zn-clay concentrate spectrum, resampled to the satellite wavelengths, showing the main Zn-OH absorption at 2257 nm (light blue line). Although the feature ~2260 nm in the EnMAP data has a small depth with respect to the noise (Fig. 11c), its magnitude seems enough to produce a mappable signal coherent with the geologic observations. Indeed, if the feature was just related to the noise, it would be spread throughout the map, and if it was a secondary feature of another phase, it should have been strongly related to another band absorption. It is

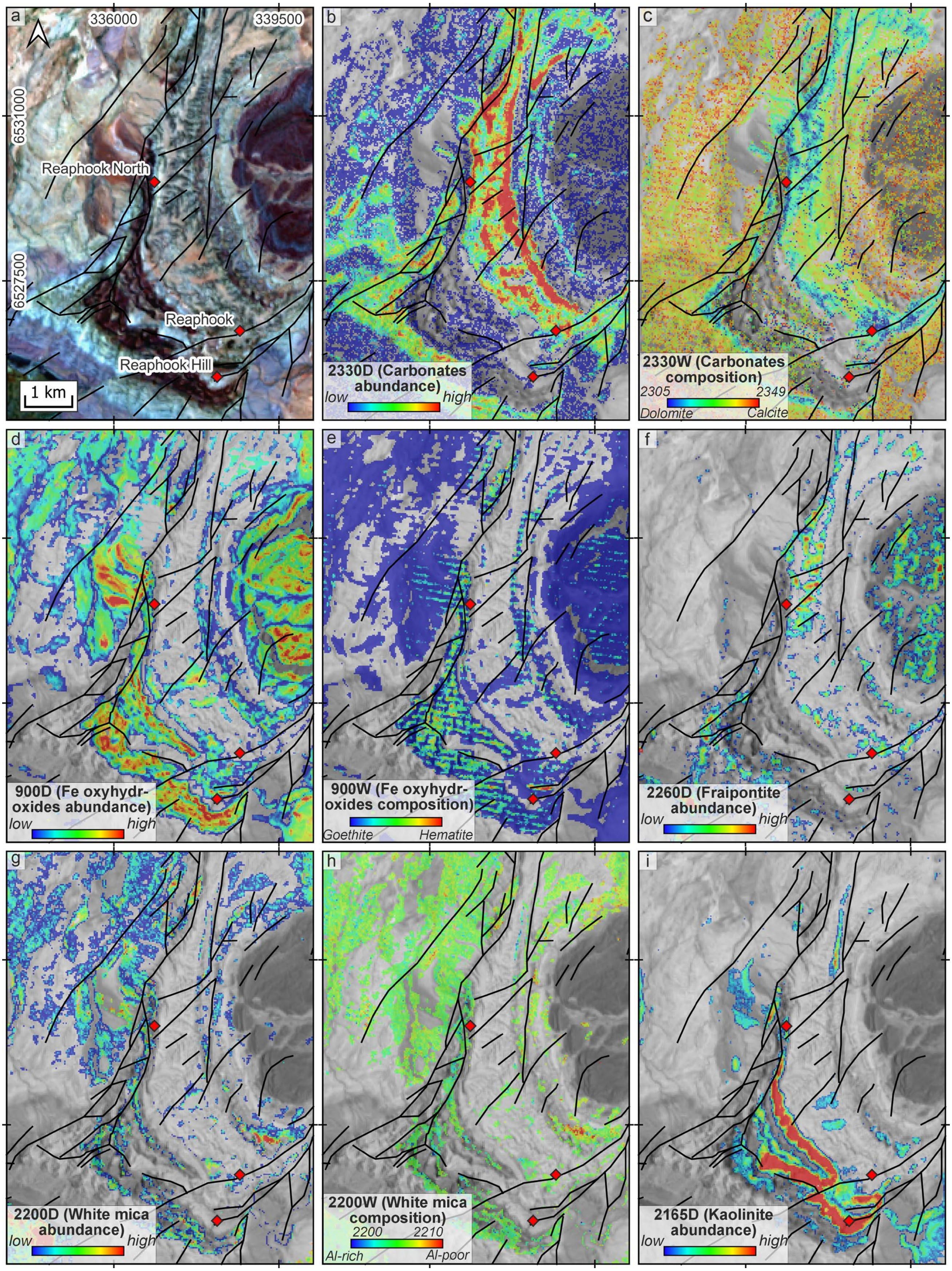
a
336000
339500
6531000
6527500
Reaphook North
Reaphook
Reaphook Hill
1 km
b
2330D (Carbonates abundance)
low
high
c
2330W (Carbonates composition)
2305
2349
Dolomite
Calcite
d
900D (Fe oxyhydr-oxides abundance)
low
high
e
900W (Fe oxyhydr-oxides composition)
Goethite
Hematite
f
2260D (Fraipontite abundance)
low
high
g
2200D (White mica abundance)
low
high
h
2200W (White mica composition)
2200
2210
Al-rich
Al-poor
i
2165D (Kaolinite abundance)
low
high

◀**Fig. 9** Mineral mapping products derived from EnMAP hyperspectral data over the Reaphook Hill area. **a** True-color composite image with the location of known mineral occurrences (red diamonds). **b** Carbonates relative abundance map (2330D). **c** Carbonates mineralogy showing variations in the minimum wavelength of 2330 nm (2330W) with calcite and dolomite at two ends. **d** Ferric iron relative abundance map (900D). **e** Ferric iron composition map (900W). **f** 2260 nm feature depth map (2260D). **g** White mica relative abundance map (2200D). **h** White mica mineralogic map (2200W) with Al-poor and Al-rich at two ends. **i** Kaolinite relative abundance map (2165D). The color-coded mineral maps are superimposed on the albedo image of the area. Solid black lines depict the faults (from Dalgarno and Johnson 1966; Preiss 1999)

evident that when investigating the co-occurrence of the ore mineral fraipontite with the alteration minerals hematite and dolomite, their three features appear to be co-located at the mineralized sites (Fig. 10a). Finally, spectra derived from quartzite, sandstone, and siltstone host rocks exhibit Al-OH absorption at ~2200 nm with subtle features at 2345 nm (Fig. 11d), related to white mica occurrences. The shift from 2199 to 2216 nm is clearly visible in EnMAP data. Moreover, the doublet absorption feature at 2165 and ~2200 nm is comparable to kaolinite (Fig. 11e).

Relationship between mineralization and tectonic structures and genetic implications

The natural color composite image of the Beltana mining area (Fig. 7a), on which fault and fractures are superimposed, shows that most orebodies are aligned along individual faults, or located in the proximity of faults intersect (Fig. 7a). In the Beltana spectral mineral maps, it is possible to see that the dolomite spectral feature was always detected proximal to the fault zones, in a NNE-SSW trend, close to mineralized areas (Fig. 7c). Moving outwards from the dolomite-rich zones, the carbonate spectral feature gradually shifts towards calcite, marking the transition to the host rock (Fig. 7c). In the Beltana area, the strongest hematite features are observed towards the eastern end, in small patches along the fault lines at the Beltana open-pit and further south at Wallrider, as well as over wider areas at Anaconda and Ajax Bore (Fig. 7e). Hematite features, surrounded by goethite haloes (Fig. 7e), were detected with dolomite along the main fault, especially in mineralized zones. In addition, these hematite-rich zones are found at the intersections of faults, or within rock volumes bounded by faults (e.g., the alteration associated with the Anaconda mineralization). Fraipontite shows the deepest absorptions (orange to red in Fig. 7f) in the Beltana fault block. In the EnMAP map of the Aroona trend, the dolomite feature appears mostly distributed across the Ajax Limestone Formation within the fault wedge bounded by the major Northwest Fault and the minor Aroona Fault, where the Aroona and Aroona II prospects are located (Fig. 8d). The dolomite feature is also common in the southernmost exposure of this limestone formation corresponding to the Mount Scott occurrences, extending along strike, and culminating towards the southeast at the periclinal termination of the antiformal fold where the North Moolooloo deposit is situated (Fig. 8d). The Reaphook North mineralization is located within an intricate structure where several faults intersect each other, whereas the Reaphook mineralization occurs on an individual fault, and Reaphook Hill near the tip point (i.e., lateral termination) of a fault (Fig. 9a). As illustrated by the carbonate spectral compositional map (Fig. 9c), dolomite-dominated pixels are mostly located close to the faults or are aligned along the faults. The strongest spectral features of fraipontite are closely correlated with those of dolomite in correspondence of mineralized sites (Fig. 9f). These observations confirm the structural control on mineral distribution (e.g. Groves et al. 2003). In addition, the close relationships between dolomite and the fault systems in this region (e.g., NW-SE faults at Aroona and NE-SW to N-S faults at Reaphook; at the branch points from North Moolooloo, to Beltana to Wallrider; Figs. 7c, 8d and 9c) allow for the discrimination between hydrothermal Fe-dolomite and diagenetic dolomite, the latter following the orientation of bedding. The dominance of the goethite signal in the Reaphook area (Fig. 9e) is consistent with the intense near-surface supergene alteration which has led to the development of ferruginous leaching caps in the mineralized zones. Even though white mica is mostly intermediate in composition, and kaolinite is highly crystalline, they likewise do not exhibit any meaningful relationships to mineralization-related hydrothermal minerals.

As recently reported by Hajaj et al. (2024), operative processing and analysis of hyperspectral data pose significant challenges due to their complexity and high dimensionality, which require the integration of statistical analyses, including machine learning and deep learning algorithms, with traditional image processing. In the PCA conducted on the mapped spectral features (i.e., 2200D, 2165D, 2330D, 900D, and 2260D), the correlation between carbonates and fraipontite is well represented by the PC2 (25.11% of explained variance), whereas in the PCA carried out on the modified database, the correlation between dolomite and fraipontite is represented by PC3 (15.51% of explained variance). In the latter, the map of the PC3 scores (see ESM) highlights the main mineralized areas well; this suggests that multivariate statistical analysis of the spectral features can be a useful tool for identifying correlations between associated minerals. However, the correlation with (hydrothermal) hematite was not significant enough to be clearly visible in the first PCs. This was likely because, considering the small scale of the

Fig. 10 **a** Co-occurrence map of dolomite, hematite, and fraipontite mineral phases over the Beltana-Aroona mineralized area. **b** Lithofacies distribution map predicted through the XGBoost machine learning algorithm

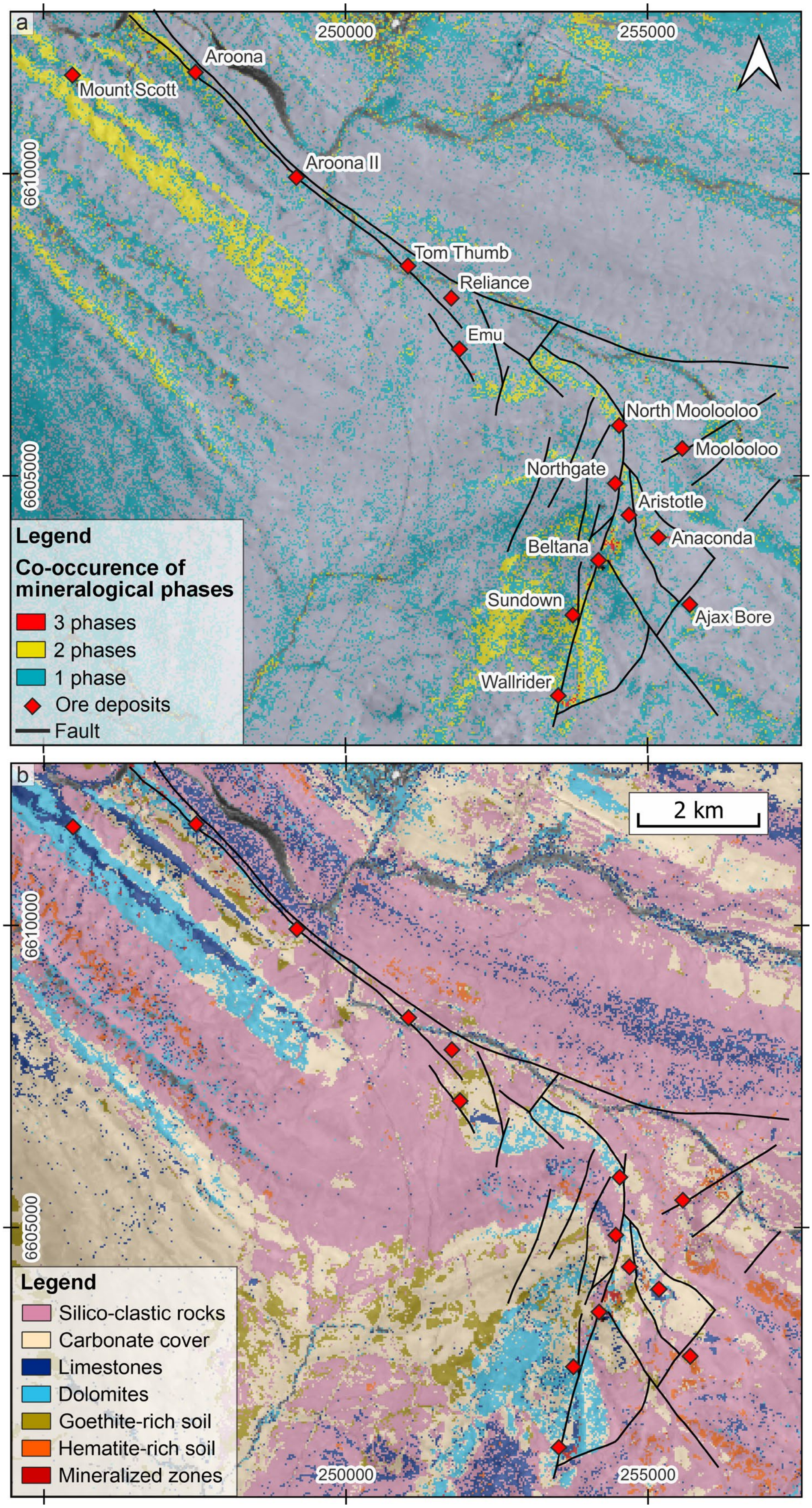

Table 3 Correlation between groups and formations identified on the Beltana-Aroona Geological map (Coats 1973), and the lithofacies predicted with the XGBoost algorithm

Groups and Formations from the Geological map			Predicted classes (%)						
			Silico-clastic rocks	Carbonate cover	Limestone	Dolomitization	Goethite-rich soil	Hematite-rich soil	Mineralized zones
	Mineralized sites		23.73	29.66	9.89	13.56	6.50	5.37	11.30
	Quaternary alluvial - colluvial deposits		48.43	35.56	5.43	4.30	5.58		
	Tertiary ferricrete and silcrete		69.21	25.93	1.39		3.01		
	Moodlatana Fm.		38.26	34.02	6.86	7.99	9.80	2.75	
	Aroona Creek Limestone		19.83	20.47	42.55	12.75	3.86		
	Billy Creek Fm.		32.29	33.22	8.16	17.62	7.97		
Hawker Gr.	Ajax Limestone*		14.10	29.37	13.21	39.64	1.12	1.32	1.26
	Parachilna Fm.		68.52	14.12	2.22	13.41	1.35		
	Uratanna Fm.		95.95	1.89				1.48	
Wilpena Gr.	Rawnsley Quartzite		82.71		6.70	5.87		3.76	
	Bonney Sandstone		57.93	19.54	4.56	8.72		8.45	
	Patsy Hill Member		46.40	41.53	1.19	7.39		2.88	
	Wonoka Fm.		6.66	83.68	7.22		1.49		
	Bunyeroo Fm.		1.35	89.52	3.48		5.18		
	ABC Range Quartzite		54.76	45.24					
	Brachina Fm.		72.04	19.71	5.50		2.27		
	Tapley Hill Fm.		13.40	56.69	27.87	1.52			
	Tindelpina Shale Member		60.41	2.04	37.55				
	Merinjina Tillite		71.23	7.40	20.62				
Burra Gr.	Bungarider SGr.	unit 1	18.34	68.41	1.27	9.96	1.99		
		unit 2	65.49	25.66	5.01	2.95			
		Myrtle Springs Fm.	16.18	59.63	9.63	13.29			
	Skillogalee Dolomite		52.48	25.63	5.18	15.13			
	Copley Quartzite		72.96		22.37	2.66		1.07	
Callanna Gr.	Curdimurka SGr.		5.51	39.76	3.96	49.74			
	Basal unit		19.12	35.91	14.51	27.37	2.41		

predicted classes % below 0.5 are not shown

*mineralized host rock

map, the combination of the three target minerals was limited to very small areas, and the features of background minerals prevailed. Machine learning methods using the XGBoost algorithm performed better than the PCA, resulting in a credible simplified lithological map of the Beltana – Aroona trend. This was achieved by automatically combining the significant spectral features obtained through the EnMAP data and mapping distinct classes (e.g., carbonate cover, silico-clastic cover, limestones, dolomites, goethite-rich soil, hematite-rich soil, and mineralized zones) identified in the Beltana mine area. The successful performance of the algorithm is related to the fact that it was set for unbalanced classes, which overcame the main limitation of the PCA which is generally designed to find the main correlations between the variables (e.g., Reimann et al. 2011). To successfully use this machine learning method to automatically process the spectral mineral maps it is necessary to have a solid training dataset, represented by a designed area with characterized geology, and covered by enough ground samples to identify the spectrally active minerals and the corresponding detectable lithofacies (Lin et al. 2023; Hajaj et al. 2024). In our case, the outcomes of the machine learning were successful as evidenced by > 80% correspondence of the lithofacies map and the geological map.

The mineralogical assemblages documented in this contribution are compatible with the genetic model of Groves et al. (2003). They suggest that the hydrothermal fluid initially precipitated hematite, which lowered the solution pH while increasing chloride ion activity. The resulting acidic, oxidized, saline fluid, with temperatures ranging from 50 to 170 °C, migrated along structural corridors, reacting with wall rocks. The intensity of hydrothermal alteration was controlled by the lithology and permeability of the host rocks. The high solubility of carbonate minerals gave rise to the extensive dolomite alteration haloes,

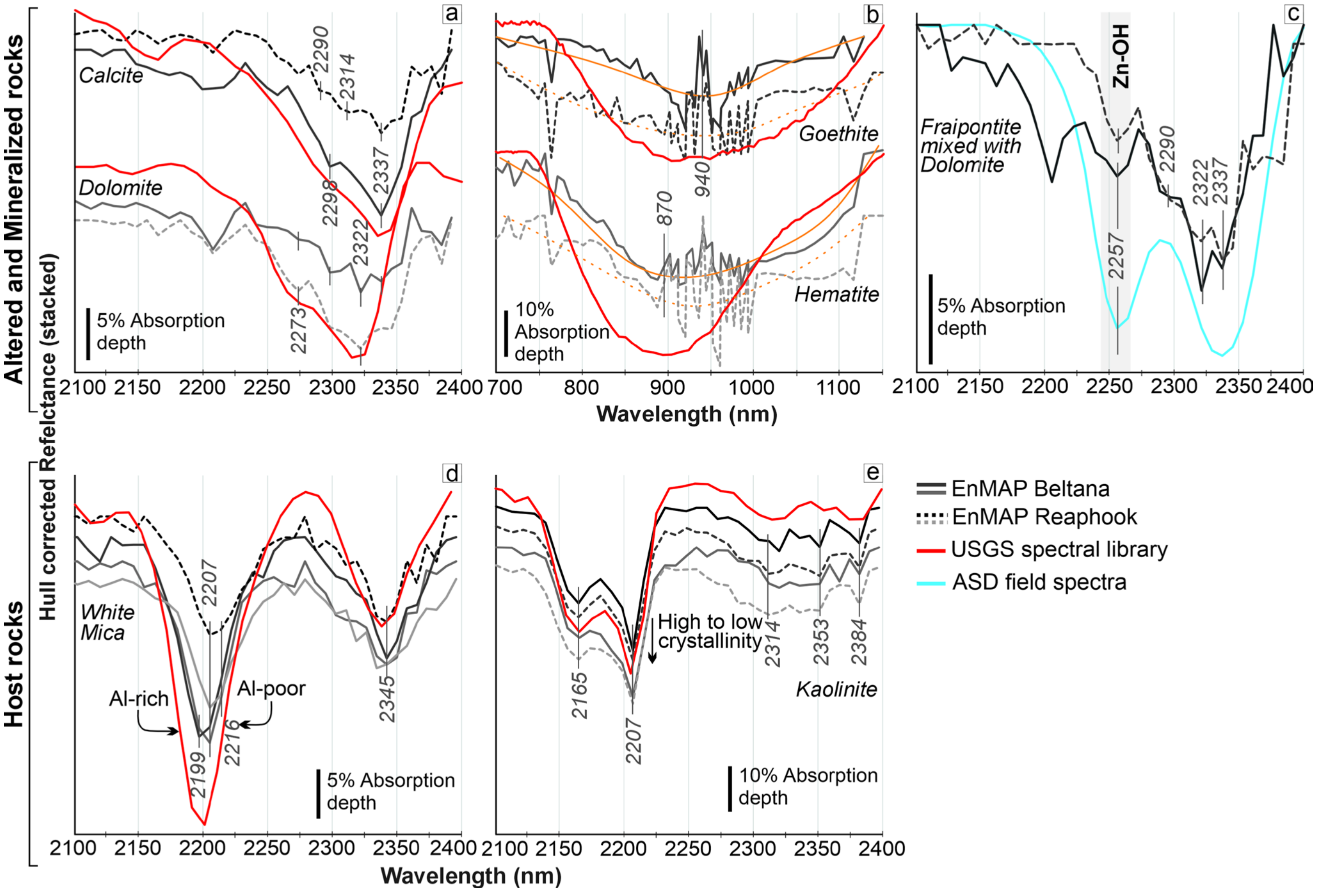

Fig. 11 Comparison between the EnMAP-derived pixel spectra with the USGS spectral library (Kokaly et al. 2017) shown in red. The pixel spectra collected from the Beltana and Reaphook areas are shown by solid and dashed grey lines, respectively. **a** calcite and dolomite. **b** goethite and hematite. **c** traces of fraipontite mixed with dolomite, compared with the spectra measured in the lab using an ASD spectrometer. **d** different species of white mica extracted from the study areas. **e** kaolinite-dominated pixels

varying from zincian dolomite accompanied by hydrothermal brecciation and dissolution near the ore (e.g., BE3.04 sample), to dolomite distal to the ore (Groves et al. 2003). The cooling and pH buffering effects of carbonate host rocks modified the pH of the fluid, bringing it towards neutral to moderately alkaline conditions and facilitating the precipitation of willemite ores in open spaces (Brugger et al. 2003; Groves et al. 2003). Given this framework, we infer that fraipontite could have directly precipitated from the mineralizing fluids, because the host rock is carbonate and would have been poor in precursor minerals that could have been directly replaced and turned into fraipontite (e.g. Putzolu et al. 2023). The flow of acidic fluids would have resulted in the dissolution of carbonates and the formation of collapse breccias, forming open space which was then filled by this Zn-clay phase. The occurrence of minor Mg-smectite could be related to a later switch from acidic to neutral pH of the mineralizing fluid.

The map patterns of the ore and alteration minerals presented in this study provide further clear evidence of the influence of faults on the genesis of the orebodies. The main mineralization and the associated hydrothermal alteration haloes are spatially associated with points of intersection between adjacent faults, volumes of rocks fully bounded by faults, and fault tips (Figs. 6, 7, 8, and 11), suggesting that fracturing enhanced the permeability, channeling the hydrothermal fluids towards the surface and facilitating wall-rock alteration and subsequent mineralization (Childs et al. 2009; Walsh et al. 2018; Camanni et al. 2021). By extrapolating in 3D, we suggest that these locations along the faults were associated with sub-vertical fluid conduits that tended to localize the upward rising ore-bearing fluids to the deposition sites, forming the associated hydrothermal alteration haloes (Fig. 12). This process could be associated with the post-Delamerian orogenesis exhumation phase as suggested by Groves et al. (2003).

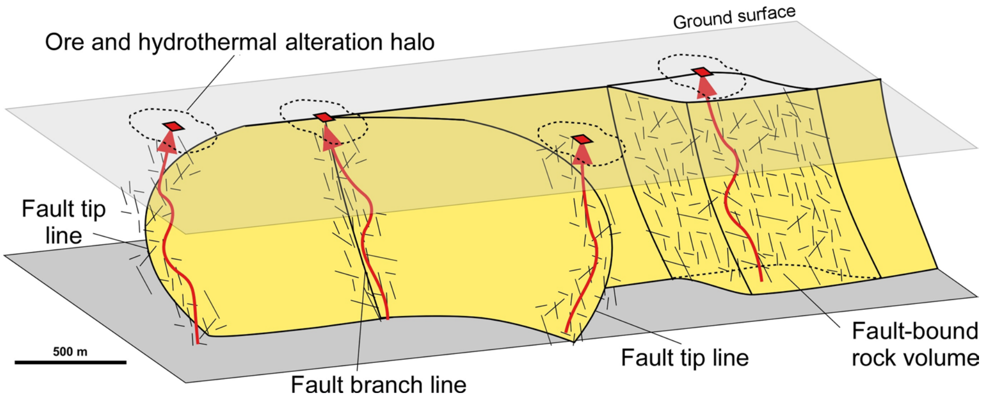

Fig. 12 Schematic model depicting the structurally-controlled fluid flow in the Flinders Ranges mineralized districts, with approximate scale. Yellow = main fault surfaces; dashed zones = pervasively fractured rock volumes; red arrows = fluid flow direction

Comparison between EnMAP and other satellite systems

Multi-spectral satellite sensors (e.g., ASTER, Landsat, and WorldView-3) have been largely used for large-scale geological mapping in similar deposit types (e.g., Gujer and Akhlamad in Iran; Ghorbani et al. 2019; Honarmand et al. 2024; Hosseini et al. 2024; Jbel Bou Dahar in Chniouar et al. 2024). However, the narrower spectral bands of EnMAP provide significant advantages, being comparable to those of airborne systems (e.g., AVIRIS, e.g., Vane et al. 1993). The higher spectral resolution allowed us to detect the chemical composition and mineralogy of several mineral phases with a higher level of confidence (e.g., Asadzadeh et al. 2024; Chakraborty et al. 2024; Jain et al. 2024). EnMAP proved remarkably effective in separating different mineral groups and discriminating spectrally similar minerals, such as dolomite and calcite, hematite, and goethite. Chirico et al. (2022) achieved comparable results in mapping alteration minerals associated with the carbonate-hosted Zn-Pb mineralization in the Jabali district (Yemen) using the ASI's PRISMA hyperspectral satellite. However, the improved signal-to-noise ratio of EnMAP, specifically in the SWIR-2 range, enables slightly more accurate mineral mapping (e.g., Chakraborty et al. 2024). For instance, it enabled the identification of the left-side shoulder of the major 2320 nm feature, centered at ~2290 nm, due to the presence of Fe in the dolomite structure. This was critical for distinguishing hydrothermal dolomite from diagenetic dolomite, particularly when combined with fault systems identification. Additionally, EnMAP enhanced the detection of subtle spectral features such as those of fraipontite at ~2260 nm for the first time. The mapping of these Zn-clays as ore minerals is recommended as it offers more precise delineation of mineralized zones compared to the sole mapping of broader alteration haloes. However, similarly to Chirico et al. (2022), the satellite data did not allow the detection of smithsonite in the mineralized areas: this was likely due to its low abundance in outcrop. Other minor challenges included the difficulty in distinguishing red willemite from iron oxides, as they share the same absorption feature. We were also unable to discriminate mineral phases with absorption features at longer wavelength positions in the SWIR-2 (e.g., scholzite and tarbuttite). This limitation is attributable to the highly noisy satellite final acquisition bands, and/or interference with the spectral signal of dominant minerals. These phases can be detected alternatively by using satellite systems including the TIR spectral bands (e.g., ASTER).

Conclusions

This study showcases the results of the first application of EnMAP hyperspectral satellite data for the mineralogical characterization and mapping of alteration footprints and ore minerals in non-sulfide Zn deposits. The work demonstrates the advantages of employing high-resolution spectral data across different spatial scales, from satellite to hand samples. In particular, the combination of point and imaging spectroscopy with traditional mineralogical analyses (i.e., XRD, FESEM-EDS) proved essential for identifying previously uncharacterized Zn-bearing minerals. A key outcome of this research is the characterization of the spectral behavior of fraipontite for the first time, achieved through specific analyses conducted on Zn-clay concentrates, highlighting Zn-OH vibrational modes at ~2260 nm. Additionally, at the hand-sample scale, the spectral signature of other Zn-bearing minerals, i.e., phosphates and carbonates, was also identified, consistent with those previously described by McConachy et al. (2007).

The surface reflectance data acquired by the hyperspectral EnMAP satellite, with its improved spectral resolution and signal-to-noise ratio, was shown to be highly useful for detecting and mapping the abundance and chemical variations of several target minerals in structurally-controlled Zn-oxidized mineralized systems. The EnMAP data effectively delineated the spatial distribution of barren host rocks and those affected by hydrothermal alteration, characterized by dolomite and hematite. It also allowed the detection of outcrops of mineralized zones, through the subtle spectral feature of Zn-clays, further demonstrating its capabilities to delineate potential targets for mineral exploration. Multivariate statistical analysis and machine learning methods were effective in highlighting correlations between key target absorption features, facilitating the analysis of the complex, high-dimensional spectral dataset. In addition, we confirmed the spatial relationship between regional faults and the location of ore deposits and their hydrothermal haloes. In particular, most mineralized zones are aligned along faults, at intersections of interacting faults, within fault-bounded rock volumes, or near lateral fault terminations, confirming that these features acted as conduits for fluid migration and mineral precipitation.

Supplementary Information The online version contains supplementary material available at https://doi.org/10.1007/s00126-025-01407-2.

Acknowledgements We are grateful to M. Boni for giving access to the sample suits from the study areas, R. De Gennaro for assistance with SEM-EDS analysis, and N. Koellner (GFZ) for her support in scanning the samples with the HySpex system. We extend our acknowledgments to the Editor-in-Chief K. Kelley and the Associate Editor M. Gadd for editorial handling, and the three anonymous reviewers for the comments that greatly enhanced the quality of the paper.

Author contributions Sorrentino, A.: Writing– original draft, Writing– review & editing, Methodology, Data curation, Investigation, Formal analysis, Software, Validation, Conceptualization. Asadzadeh, S.: Writing– review & editing, Methodology, Formal analysis, Software. Camanni, G.: Writing– review & editing, Formal analysis. Carotenuto, F.: Writing– review & editing, Formal analysis. Chabrillat, S.: Writing– review & editing. Gleeson, S.: Writing– review & editing. Balassone, G.: Writing– review & editing, Formal analysis. Mondillo, N.: Writing– review & editing, Conceptualization; Supervision; Funding.

Funding Open access funding provided by Università degli Studi di Napoli Federico II within the CRUI-CARE Agreement. This research was produced in the frame of the Ph.D. project of A. Sorrentino (Ph.D. scholarships of the Programma Operativo Nazionale - PON "Research and Innovation 2014–2020"), co-financed by the Italian Ministry of University and Research and European Social Fund (ESF) 2014–2020, under the Supervision of Nicola Mondillo. S.A.G. is funded by a Helmholtz Association Recruitment Initiative and a Taighde Éireann – Research Ireland Professorship under Grant number 23/RP/12193. S.A. received funding from the EnMAP science program (grant number 50EE2401).

Data Availability All EnMAP data are freely available through the EnMAP data access portal at the following link: https://www.enmap.org/data_access/. The EnMAP data are licensed products of DLR [2023–2024], all rights reserved.

Declarations

Competing interests The authors declare no competing financial interests or personal relationships that could have appeared to influence the work reported in this paper.

References

Asadzadeh S, Souza Filho CR (2016) Iterative curve fitting: a robust technique to estimate the wavelength position and depth of absorption features from spectral data. IEEE Trans Geosci Remote Sens 54:5964–5974

Asadzadeh S, Zhou X, Chabrillat S (2024) Assessment of the spaceborne enmap hyperspectral data for alteration mineral mapping: a case study of the Reko Diq porphyry CuAu deposit, Pakistan. Remote Sens Environ 314:114389

Bedini E (2017) The use of hyperspectral remote sensing for mineral exploration: a review. J Hyperspect Remote Sens 7:189–211

Brugger J, McPhail DC, Wallace M, Waters J (2003) Formation of willemite in hydrothermal environments. Econ Geol 98:819–835

Burns RG (1993) Mineralogical applications of crystal field theory. Second edition. Cambridge University Press; Cambridge Topics in Miner Phys Chem, 5

Camanni G, Vinci F, Tavani S et al (2021) Fracture density variations within a reservoir-scale normal fault zone: a case study from shallow-water carbonates of Southern Italy. J Struct Geol 151:104432

Carman C, Groves I (2003) Geophysics as an exploration tool for willemite-a case study of the Beltana-Reliance-Aroona zinc deposits, Northern Flinders Ranges, South Australia. ASEG Ext Abstr 2003:223–231

Chabrillat S, Foerster S, Segl K et al (2024) The EnMAP spaceborne imaging spectroscopy mission: initial scientific results two years after launch. Remote Sens Environ. https://doi.org/10.1016/j.rse.2024.114379

Chakraborty R, Rachdi I, Thiele S et al (2024) A spectral and spatial comparison of satellite-based hyperspectral data for geological mapping. Remote Sens 16:2089

Chen T, Guestrin C (2016) XGBoost: a scalable tree boosting system. In: Proceedings of the 22nd acm sigkdd international conference on knowledge discovery and data mining. ACM, San Francisco California USA, pp 785–794

Childs C, Manzocchi T, Walsh JJ et al (2009) A geometric model of fault zone and fault rock thickness variations. J Struct Geol 31:117–127

Chirico R, Mondillo N, Laukamp C et al (2022) Mapping hydrothermal and supergene alteration zones associated with carbonate-hosted Zn-Pb deposits by using PRISMA satellite imagery supported by field-based hyperspectral data, mineralogical and geochemical analysis. Ore Geol Rev 105244

Chniouar M, Wafik A, Daafi Y, Guglietta D (2024) Integrated remote sensing for geological and mineralogical mapping of Pb-Zn deposits: a case study of Jbel Bou Dahar region using multi-sensor imagery. Mining 4:302–325

Choulet F, Buatier M, Barbanson L, Guégan R, Ennaciri A (2016) Zinc-rich clays in supergene non-sulfide zinc deposits. Mineral Deposita 51:467–490

Coats RP (1973) Copley South Australia explanatory notes, 1: 250,000 geological series. sheet SH/54 – 9 international index

Cogliati S, Sarti F, Chiarantini L et al (2021) The PRISMA imaging spectroscopy mission: overview and first performance analysis. Remote Sens Environ 262:112499

Coppola V, Boni M, Gilg HA, Balassone G, Dejonghe L (2008) The calamine nonsulfide Zn–Pb deposits of Belgium: petrographical, mineralogical and geochemical characterization. Ore Geol Rev 33:187–210

Corrado F, Putzolu F, Armstrong RN et al (2025) Application of satellite and proximal hyperspectral sensing to target lithium mineralization in volcano-sedimentary deposits: a case study from the McDermitt caldera, USA. Remote Sens Environ 323:114724

Cowley WM (2020) Geological setting of exceptional geological features of the Flinders Ranges. Aust J Earth Sci 67(6):763–785. https://doi.org/10.1080/08120099.2020.1748109

Cox SF (2005) Coupling between deformation, fluid pressures, and fluid flow in ore-producing hydrothermal systems at depth in the crust. Econ Geol 100th Anniversary Volume:39–75. https://doi.org/10.5382/AV100.04

Cox SF, Knackstedt MA, Braun J (2001) Principles of structural control on permeability and fluid flow in hydrothermal systems. Rev Econ Geol 14:1–24

Crowley J, Williams D, Hammarstrom J et al (2003) Spectral reflectance properties (0.4–2.5 μm) of secondary Fe-oxide, Fe-hydroxide, and Fe-sulphate-hydrate minerals associated with sulphide-bearing mine wastes. Geochem Explor Environ Anal 3:219–228

Cudahy T, Jones M, Thomas M et al (2008) Next generation mineral mapping: Queensland airborne HyMap and satellite ASTER surveys 2006–2008. Commonwealth Scientific and Industrial Research Organization Report P2007/364. https://doi.org/10.13140/RG.2.1.2828.1844

Dalgarno CR, Johnson JE (1966) PARACHILNA map sheet, Geological Atlas of South Australia, 1: 250 000 series. Geol Surv S Aust

Dyson IA (2001) The diapir-base metal association in the Northern Flinders ranges. MESA J 22:37–43

Elliott P (2022) Reaphookhillite, MgZn2 (PO4) 2· 4H2O, the Mg analogue of parahopeite from reaphook Hill, South Australia. Mineral Mag 86:525–530

Foden J, Elburg MA, Dougherty-Page J, Burtt A (2006) The timing and duration of the Delamerian orogeny: correlation with the Ross orogen and implications for Gondwana assembly. JourGeol 114:189–210. https://doi.org/10.1086/499570

Gaffey SJ (1986) Spectral reflectance of carbonate minerals in the visible and near infrared (0.35–2.55 microns); calcite, aragonite, and dolomite. Am Mineral 71:151–162

Ghorbani A, Honarmand M, Shahriari H, Hassani MJ (2019) Regional scale prospecting for non-sulphide zinc deposits using ASTER data and different spectral processing methods. Int J Remote Sens 40:8647–8667. https://doi.org/10.1080/01431161.2019.1620372

Green RO, Mahowald N, Ung C et al (2020) The Earth surface mineral dust source investigation: an earth science imaging spectroscopy mission. In: 2020 IEEE aerospace conference. IEEE, pp 1–15

Groves IM, Carman CE, Dunlap WJ (2003) Geology of the Beltana Willemite deposit, Flinders Ranges, South Australia. Econ Geol 98:797–818

Guanter L, Kaufmann H, Segl K et al (2015) The enmap spaceborne imaging spectroscopy mission for Earth observation. Remote Sens 7:8830–8857

Haest M, Cudahy T, Laukamp C, Gregory S (2012) Quantitative mineralogy from infrared spectroscopic data. I. Validation of mineral abundance and composition scripts at the Rocklea channel iron deposit in Western Australia. Econ Geol 107:209–228

Hajaj S, El Harti A, Pour AB et al (2024) A review on hyperspectral imagery application for lithological mapping and mineral prospecting: machine learning techniques and future prospects. Remote Sens Appl Soc Environ. https://doi.org/10.1016/j.rsase.2024.101218

Harkins SA, Appold MS, Nelson BK et al (2008) Lead isotope constraints on the origin of nonsulfide zinc and sulfide zinc-lead deposits in the Flinders Ranges, South Australia. Econ Geol 103:353–364

Hijmans RJ (2025) Package ‘terra’: Spatial data analysis. Contributed Packages, CRAN

Hill RJ (1973) Scholzite and other phosphate minerals from Reaphook Hill, South Australia. Neues Jahrbuch für Mineralogie - Monatshefte 1973:1–8. https://doi.org/10.1127/njmm/1973/1973/1

Hill RJ, Milnes AR (1974) Phosphate minerals from Reaphook Hill, Flinders Ranges, South Australia. Mineral Mag 39:684–695

Hitzman MW, Reynolds NA, Sangster D et al (2003) Classification, genesis, and exploration guides for nonsulfide zinc deposits. Econ Geol 98:685–714. https://doi.org/10.2113/gsecongeo.98.4.685

Honarmand M, Shahriari H, Zadeh MH, Ghorbani A (2024) Enhancing Zn-bearing gossans from GeoEye-1 and Landsat 8 OLI data for non-sulphide Zn deposit exploration. Egypt J Remote Sens Space Sci 27:93–107

Hosseini S, Gholamzadeh M, Pour AB et al (2024) Multi-sensor satellite remote-sensing data for exploring carbonate-hosted Pb-Zn mineralization: Akhlamad area, Razavi Khorasan, north east Iran. Mining 4:367–388

Hunt GR (1977) Spectral signatures of particulate minerals in the visible and near infrared. Geophysics 42:501–513. https://doi.org/10.1190/1.1440721

Jain R, Bhu H, Pandey AK, Pour AB (2024) Base-metal exploration by using remote sensing, geological, geophysical, and geochemical datasets with clues from ancient mining: a comprehensive review on Aravalli-Delhi Fold Belt, Rajasthan, India. Advances in Space Research

Jenkins RJF (1990) The Adelaide fold belt: tectonic reappraisal. The evolution of a late Precambrian-Early paleozoic rift complex: the Adelaide geosyncline: geological. Soc Australia Special Publication 16:396–420

Kokaly R, Clark R, Swayze G et al (2017) Usgs spectral library version 7 data: US geological survey data release. United States Geological Survey (USGS): Reston, VA, USA 61

Krutz D, Müller R, Knodt U et al (2019) The instrument design of the DLR Earth sensing imaging spectrometer (DESIS). Sensors (Basel) 19:1622

Kuhn M (2008) Building predictive models in R using the caret package. J Stat Softw 28:1–26

Lampinen HM, Laukamp C, Occhipinti SA, Hardy L (2019) Mineral footprints of the paleoproterozoic sediment-hosted Abra Pb-Zn-Cu-Au deposit Capricorn Orogen, Western Australia. Ore Geol Rev 104:436–461

Laukamp C, Rodger A, LeGras M et al (2021) Mineral physicochemistry underlying feature-based extraction of mineral abundance and composition from shortwave, mid and thermal infrared reflectance spectra. Minerals 11:347

Laukamp C, Termin KA, Pejcic B et al (2012) Vibrational spectroscopy of calcic amphiboles–applications for exploration and mining. Eur J Mineral 24:863–878

Lin N, Fu J, Jiang R et al (2023) Lithological classification by hyperspectral images based on a two-layer XGBoost model, combined with a greedy algorithm. Remote Sens 15:3764

McConachy TF, Yang K, Boni M, Evans NJ (2007) Spectral reflectance: preliminary data on a new technique with potential for non-sulphide base metal exploration. Geochem Explor Environ Anal 7:139–151

Mondillo N, Nieto F, Balassone G (2015) Micro-and nano-characterization of Zn-clays in nonsulfide supergene ores of Southern Peru. Am Mineral 100:2484–2496

Monteiro LVS, Bettencourt JS, Juliani C, de Oliveira TF (2006) Geology, petrography, and mineral chemistry of the Vazante non-sulfide and Ambrósia and Fagundes sulfide-rich carbonate-hosted Zn–(Pb) deposits, Minas Gerais, Brazil. Ore Geol Rev 28:201–234

Muller DW (1972) The geology of the Beltana Willemite deposits. Econ Geol 67:1146–1167

Newman ACD, Brown G (1987) The chemical constitution of clays

Olivo GR, Monteiro LV, Baia F et al (2018) The Proterozoic Vazante hypogene zinc silicate district, Minas Gerais, Brazil: a review of the ore system applied to mineral exploration. Minerals 8:22

Preiss WV (1999) Parachilna, South Australia, sheet SH54-13 1: 250 000 geological series explanatory notes . Geol Surv S Aust

Preiss WV (2000) The Adelaide geosyncline of South Australia and its significance in neoproterozoic continental reconstruction. Precambrian Res 100:21–63

Putzolu F, Abad I, Balassone G, Boni M, Lupo F, Mondillo N (2023) Zn-clays in the Kihabe and Nxuu prospects (Aha Hills, Botswana): a XRD and TEM study. Am Mineral 108:362–382

R Core Team (2024) R: A Language and environment for statistical computing. R Foundation for Statistical, Computing https://www.r-project.org

Reimann C, Filzmoser P, Garrett R, Dutter R (2011) Statistical data analysis explained: applied environmental statistics with R. John Wiley & Sons

Rodger A, Laukamp C, Haest M, Cudahy T (2012) A simple quadratic method of absorption feature wavelength estimation in continuum removed spectra. Remote Sens Environ 118:273–283

Rowan MG, Vendeville BC (2006) Foldbelts with early salt withdrawal and diapirism: physical model and examples from the Northern Gulf of Mexico and the Flinders Ranges, Australia. Mar Pet Geol 23:871–891

Rutland RWR, Parker AJ, Pitt GM et al (1981) The Precambrian of South Australia. Developments in Precambrian Geology. Elsevier, pp 309–360

Sabins FF (1999) Remote sensing for mineral exploration. Ore Geol Rev 14:157–183

Savitzky A, Golay MJ (1964) Smoothing and differentiation of data by simplified least squares procedures. Anal Chem 36:1627–1639

Sibson RH (2001) Seismogenic framework for hydrothermal transport and ore deposition. Reviews Economic Geol 14:25–50. https://doi.org/10.5382/Rev.14.02

Sonntag I, Laukamp C, Hagemann SG (2012) Low potassium hydrothermal alteration in low sulfidation epithermal systems as detected by IRS and XRD: an example from the Co–O mine, Eastern Mindanao, Philippines. Ore Geol Rev 45:47–60

Sorrentino A, Chirico R, Corrado F et al (2024) The application of PRISMA hyperspectral satellite imagery in the delineation of distinct hydrothermal alteration zones in the Chilean Andes: the Marimaca IOCG and the Río Blanco-Los Bronces Cu-Mo porphyry districts. Ore Geol Rev. https://doi.org/10.1016/j.oregeorev.2024.105998

Storch T, Honold H-P, Chabrillat S et al (2023) The enmap imaging spectroscopy mission towards operations. Remote Sens Environ 294:113632

Swayze GA, Clark RN, Goetz AFH et al (2003) Effects of spectrometer band pass, sampling, and signal-to-noise ratio on spectral identification using the tetracorder algorithm. J Geophys Res 108:2002JE001975. https://doi.org/10.1029/2002JE001975

Tan W, He H, Chen X, Qi W (2020) Analyzing the influence of atmosphere on optical remote sensing in 400 to 2500 nm wavelength spectrum. In: AOPC 2020: Optical Spectroscopy and Imaging; and Biomedical Optics. SPIE, pp 103–108

Taranik JV, Aslett ZL (2009) Development of hyperspectral imaging for mineral exploration. In: Bedell R, Crósta AP, Grunsky E (eds) Remote Sensing and Spectral Geology. Society of Economic Geologists, p 0

Thiele ST, Lorenz S, Kirsch M, et al (2021) Multi-scale, multi-sensor data integration for automated 3-D geological mapping. Ore Geol Rev 136:104252 https://doi.org/10.1016/j.oregeorev.2021.104252

Thomson BP (1976) Late Precambrian and Cambrian Geology of the Adelaide Geosyncline and Stuart Shelf, South Australia, 33rd edn. 25th International Geological Congress

Van Der Meer F (1995) Spectral reflectance of carbonate mineral mixtures and bidirectional reflectance theory: quantitative analysis techniques for application in remote sensing. Remote Sens Rev 13:67–94. https://doi.org/10.1080/02757259509532297

Van Ruitenbeek FJ, Bakker WH, van der Werff HM, et al (2014) Mapping the wavelength position of deepest absorption features to explore mineral diversity in hyperspectral images. Plan Space Sci 101:108–117 https://doi.org/10.1016/j.pss.2014.06.009

Vane G, Green RO, Chrien TG, Enmark HT, Hansen Eg, Porter WM (1993) The airborne visible/infrared imaging spectrometer (AVIRIS). Remote Sens Environ 44:127–143

Velde B (1965) Phengite micas; synthesis, stability, and natural occurrence. Am J Sci 263:886–913

Walsh JJ, Torremans K, Güven J et al (2018) Fault-controlled fluid flow within extensional basins and its implications for sedimentary rock-hosted mineral deposits. Soc Economic Geol Special Publication 21:11